EMT activates ER-to-Golgi trafficking through upregulation of REEP2 to promote lung cancer progression

Kevin Fulp[1, 7], Oluwafunminiyi Obaleye[1, 7], Shike Wang[2], Xin Liu[3], Jiang Yu[3], Jonathan M. Kurie[3], Jun Xu[5], William K. Russell[6], Xiaochao Tan[2, *], Guan-Yu Xiao[1, *]

[1] Department of Toxicology and Cancer Biology, The University of Kentucky College of Medicine, Lexington, Kentucky; [2]Department of Medicine, Tulane University School of Medicine, Louisiana Cancer Research Center, New Orleans, Louisiana; [3]Department of Thoracic/Head and Neck Medical Oncology, The University of Texas MD Anderson Cancer Center, Houston, Texas; [4]Department of Molecular and Cellular Oncology, The University of Texas MD Anderson Cancer Center, Houston, Texas; [5]Department of Biochemistry and Molecular Biology, Baylor College of Medicine, Houston, Texas; [6]Department of Biochemistry and Molecular Biology, University of Texas Medical Branch, Galveston, Texas. [7]These authors contributed equally: Kevin Fulp, Oluwafunminiyi Obaleye.

*To whom correspondence should be addressed: Xiaochao Tan, Department of Medicine, Tulane University School of Medicine, New Orleans, LA 70112, USA; email: xtan4@tulane.edu; Guan-Yu Xiao, Department of Toxicology and Cancer Biology, University of Kentucky, Lexington, KY 40508, USA. Email: guan-yu.xiao@uky.edu.

Abstract

Membrane trafficking governs the transport of molecules to both intracellular and extracellular locations, thereby maintaining cell homeostasis. During cancer progression, alterations in membrane trafficking are frequently observed. However, the mechanisms underlying the dysregulation of membrane trafficking in cancer progression remain largely unresolved. Recent

evidence has demonstrated that epithelial-to-mesenchymal transition (EMT) in lung adenocarcinoma (LUAD) employs a membrane trafficking program to coordinate cancer cell invasion and immunosuppression in the tumor microenvironment (TME). To further dissect the pro-tumorigenic membrane trafficking program, here we conducted a CRISPR interference (CRISPRi) *in vivo* screen for membrane trafficking regulators in a syngeneic mouse model with a complete immune system. This screen identified REEP2, an endoplasmic reticulum (ER) shaping protein, as a novel regulator of the EMT-dependent membrane trafficking program, which is associated with a poor prognosis in LUAD patients and is required for LUAD metastasis in a syngeneic orthotopic LUAD mouse model. Mechanistically, the EMT activator ZEB1 upregulates REEP2 expression through miR-183- and miR-193a-mediated regulation that promotes the transportation of secretory cargoes from the ER exit site (ERES) to the Golgi, thereby augmenting the secretion of pro-tumorigenic factors. The REEP2-driven secretion promotes cancer cell proliferation, migration, and the infiltration of myeloid-derived suppressor cells (MDSCs) in the TME. These findings identify REEP2 as a critical mediator of the EMT-driven pro-metastatic membrane trafficking program, revealing a specific vulnerability in mesenchymal LUAD.

Introduction

Membrane trafficking, a highly regulated process that is essential for cellular homeostasis, is disrupted on multiple levels in cancer, framing a new frontier in targeted therapeutics for cancer treatments [1-7]. It involves the complex coordination of a host of vesicles shuttling an array of cargo to and from the endoplasmic reticulum (ER), Golgi apparatus, the plasma membrane, and extracellular space [5-8]. Numerous cancer-associated mutations have been identified in the components of the membrane trafficking machinery [9,10]. Furthermore, cancer cells coordinate membrane trafficking components post-transcriptionally (i.e. microRNA regulation) [11-14] and post-translationally (i.e. phosphorylation) [15-20] to dynamically adapt membrane trafficking pathways and acquire metastatic capabilities. Although numerous genome-wide analyses have been performed

53 to interrogate the roles of membrane trafficking components in cancer cells [21,22], many critical
54 knowledge gaps remain regarding the mechanisms of their dysregulation in cancer progression,
55 and this area continues to be fertile ground for the discovery of novel cancer treatments.

56 Recent studies reveal that epithelial-to-mesenchymal (EMT)-activating transcription factors
57 coordinate membrane trafficking networks to establish a front-rear polarity axis that facilitates
58 cancer cell motility [14,23]. Importantly, the EMT-driven membrane trafficking program underlies a
59 vulnerability of EMT-driven metastatic cancers [11,12], and the inhibition of EMT-activated
60 membrane trafficking regulators reactivates anti-tumor immunity in the tumor microenvironment
61 (TME) and reverses acquired resistance to immune checkpoint inhibitor (ICI) therapy in LUAD [11].
62 However, no comprehensive studies have systematically examined how membrane trafficking
63 machinery influences TME that is essential for cancer progression.

64 To identify the membrane trafficking regulators critical for tumor growth with immune selective
65 pressure, here we conducted a CRISPR repression (CRISPRi) *in vivo* screen in a syngeneic
66 mouse model. Using LUAD cell lines derived from humans and genetically engineered mice that
67 develop metastatic LUAD, which are classified as epithelial or mesenchymal [11,24-26] (Table S1),
68 we further investigated regulatory mechanisms of the identified candidate, REEP2, an
69 endoplasmic reticulum (ER) shaping protein, in membrane trafficking and LUAD progression. The
70 findings presented herein uncover a molecular underpinning by which EMT promotes the
71 secretory cargo transportation from the ER exit site (ERES) to the Golgi and, in turn, enhances
72 the secretion of pro-tumorigenic factors that foster cancer cell motility and immunosuppressive
73 TME.

74

75 **Results**

76 **Pro-tumorigenic membrane trafficking program for LUAD growth**

77 To systematically characterize the EMT-driven membrane trafficking in LUAD progression and
78 immunosuppression, we transduced a CRISPR interference (CRISPRi) library targeting 2,099

79 trafficking-related genes [27] into murine mesenchymal LUAD 344SQ cells, which develop into
80 metastatic LUADs owing to high expression of the EMT activator, ZEB1 [26] (Fig. 1A). We performed
81 an *in vivo* screen by transplanting the cells into syngeneic wild-type (WT) immunocompetent
82 mouse flanks and measured the effects on tumorigenesis (Fig. 1A). This screen revealed a panel
83 of membrane trafficking regulators required for tumor growth under immune surveillance (fold-
84 change (log_2) < -1, FDR ($-log_{10}$) > 20) (Fig. 1B, blue box, Table S2). We prioritized a set of top
85 hits (fold-change (log_2) < -2 and FDR ($-log_{10}$) > 20, Fig. 1B, red dots and Fig. 1C) and assessed
86 their correlation with EMT (Fig. 1D) and prognostic values (Fig. 1E and Fig. S1) using The Cancer
87 Genome Atlas (TCGA) database. We identified several membrane trafficking regulators (*KRT16,*
88 *REEP2, TNNT1, ARL14*) that significantly correlate with the EMT signature and shorter survival
89 durations of LUAD patients. These findings reveal a membrane trafficking program that
90 contributes to LUAD tumorigenesis. Among these hits, REEP2 represents the strongest EMT
91 correlation and demonstrates high prognostic value, and correlates with LUAD metastasis (Fig.
92 1F).
93
94 **REEP2 is required for mesenchymal LUAD metastasis**
95 To further investigate the function of REEP2 in LUAD progression, we subjected murine
96 mesenchymal 344SQ cells to CRISPR/Cas9-mediated REEP2 knockout (REEP2 KO) (Fig. S2A),
97 and inoculated the cells orthotopically in the lungs of the syngeneic WT mice. We found that
98 REEP2 KO cells generated orthotopic LUADs that were smaller (Fig. 2A, left dot plot) and less
99 metastatic to the mediastinum (Fig. 2A, middle dot plot) and the contralateral lung (Fig. 2A, right
100 dot plot). We then assessed cancer progression properties *in vitro* and found that REEP2
101 depletion (Fig. S2A-D) reduced murine (344SQ) and human (H1299) mesenchymal LUAD cell
102 proliferation (Fig. 2B), but negligibly affected the viability of human epithelial LUAD (HCC827) (Fig.
103 S2E) or non-cancerous human bronchial epithelial cell (HBEC30KT) (Fig. S2F). Furthermore, we
104 found that REEP2 deficiency in mesenchymal LUAD cells resulted in cell cycle arrest (Fig. 2C),

105 with a negligible change in apoptosis (Fig. 2D), and sharply reduced migratory and invasive
106 activities in Boyden chambers (Fig. 2E and F). These data indicate a significant, previously
107 unknown association of REEP2 with LUAD progression.
108
109 **ZEB1 relieves REEP2 from microRNA-dependent silencing**
110 We identified a positive correlation between ZEB1 and REEP2 expressions in human LUAD
111 (Fig. 3A) and validated that their mRNA and protein levels changed in a corresponding fashion
112 following ZEB1 gain- or loss-of-function (Fig. 3B, S3A). ZEB1 has been shown to silence
113 microRNAs (miRs) to relieve the negative transcriptional regulation from genes involved in LUAD
114 progression [11,14,24,25]. Using the TargetScan prediction tool (www.targetscan.org), we identified
115 predicted miR-183 and miR-193a binding sites on the REEP2 3'-untranslated regions (3'-UTRs)
116 (Fig. S3B). In the epithelial cells with inducible ZEB1 expression (H322_iZEB1), ZEB1 induction
117 repressed the expressions of both miR-183 and miR-193a, while upregulating REEP2
118 simultaneously (Fig. S3C). We found that miR-183 and miR-193a mimics reduce REEP2
119 expression in murine and human mesenchymal LUAD cells (Fig. 3C, S3D). To validate the miR-
120 183- and miR-193a-mediated REEP2 silencing, we mutated the predicted binding sites (Fig. S3B)
121 and found that both miR-183 and miR-193a mimics suppressed the activity of human REEP2
122 reporters containing wild-type but not mutant 3'-UTRs lacking predicted binding sites (Fig. 3D and
123 E). These findings define a REEP2 regulatory axis in which ZEB1 alleviates miRNA-mediated
124 repression, leading to REEP2 upregulation in mesenchymal LUAD.
125
126 **ZEB1 coordinates REEP2 to promote ERES and Golgi colocalization in mesenchymal**
127 **LUAD**
128 REEP proteins are known to generate membrane curvature of the ER to regulate its structure
129 and function [28] and have been suggested to function in secretory trafficking [29]. Proteins destined
130 for secretion are synthesized in the ER, where cargoes are packaged into ERES and transferred

131 to the Golgi apparatus [30], after which they are directed to the plasma membrane through post-
132 Golgi traffic [31]. SEC proteins, including SEC16 and SEC24, are recruited to the site of ERES and
133 are essential for the formation of ERES and cargo packaging [32-34]. GM130 at the cis-Golgi tethers
134 ERES cargo delivery to the Golgi [35]. Given the significant curvature at the ERES, we hypothesized
135 that ZEB1 coordinates REEP2 to direct ERES toward the Golgi in mesenchymal LUAD (Fig. 4A).
136 To test the possibility, we visualized the distribution of SEC16A and GM130 using
137 immunofluorescence. Strikingly, compared to empty vector control (Vec), which showed the
138 dispersed SEC16A signals outside of the Golgi area marked by GM130 (Fig. S4A, arrows),
139 ectopic ZEB1 expression remarkably increased SEC16A colocalization with GM130 (Fig. S4A,
140 arrowheads) in the epithelial murine (393P) LUAD cells. The depletion of ZEB1 in the
141 mesenchymal murine (344SQ) and human (H1299) LUAD cells reduced the SEC16A/GM130
142 colocalization (Fig. S4B and C). The deficiency of REEP2 similarly decreased their colocalization
143 in the mesenchymal human (H1299) LUAD cells (Fig. S4C). Furthermore, the ectopic expression
144 of ZEB1 in the epithelial human (HCC827) LUAD cells increased the SEC16A/GM130
145 colocalization (Fig. 4B, Vec vs. siCTL), while REEP2 depletion (Fig. S4D) abolished the
146 phenotype (Fig. 4B, siCTL vs. siREEP2s). We then observed the consistent findings of higher
147 colocalization between SEC24D-labelled ERES and the Golgi in the epithelial human (HCC827)
148 LUAD cells with ectopic ZEB1 expression compared to Vec (Fig. 4C), while REEP2 depletion
149 disrupted the phenotype (Fig. 4D), suggesting ZEB1 coordinates REEP2 to promote ERES
150 locating on the Golgi in mesenchymal LUAD.

151 Thus far, REEP2 was observed to form vesicular structures that lack colocalization with
152 markers of canonical cellular compartments [36]. To further investigate the distribution and function
153 of REEP2, we transfected the HCC827 cells with fluorescent-tagged REEP2 (Fig. S4E) and found
154 that the REEP2 vesicles highly colocalized with SEC24D-labelled ERES (~80%) and there was
155 no difference between ectopic Vec and ZEB1 expression (Fig. S4F). However, the ectopic
156 expression of ZEB1 significantly enhanced the ERES colocalization with the Golgi (Fig. 4E).

157 Strikingly, we observed that the SEC24D structures with REEP2 coating dramatically increased
158 their colocalization with the Golgi, compared to those lacking REEP2 coating, and ectopic ZEB1
159 expression further raised the colocalization (Fig. 4F). These findings suggest that REEP2
160 recruitment to the ERES is necessary for their transportation to the Golgi.
161
162 **REEP2-driven ERES/Golgi colocalization promotes secretory trafficking**
163 To test how REEP2-driven ERES/Golgi colocalization influences protein trafficking, we used
164 the retention using selective hooks (RUSH) system [37] to quantitatively monitor trafficking kinetics
165 at different time points. Human mesenchymal LUAD cells (H1299) were transfected with a GFP-
166 tagged CD-MPR, a canonical cargo that localizes to the trans-Golgi network (TGN) [38], which binds
167 to streptavidin fusing with an ER retention signal (Lys-Asp-Glu-Leu; KDEL) via the streptavidin-
168 binding peptide (SBP) (Fig. S5A). Upon biotin treatment, the CD-MPR-RUSH is released from the
169 ER and trafficked to the Golgi (Fig. 5A, siCTL, S5A). REEP2 depletion drastically reduced the
170 trafficking of CD-MPR-RUSH to the Golgi at both 10 minutes and 30 minutes post-Biotin treatment
171 (Fig. 5A).
172 Next, to assess whether ERES/Golgi colocalization facilitates secretory trafficking, the ER
173 stress inducer, thapsigargin, was used to disperse SEC16A [34], and the temperature-sensitive
174 mutant vesicular stomatitis virus (VSV-G) assay was used to measure secretory trafficking (Fig.
175 S5B). Consistent with the previous study [34], thapsigargin disrupted ERES colocalization with the
176 Golgi (Fig. S5C). We observed that the reduced ERES/Golgi colocalization impacted secretory
177 trafficking in the mesenchymal human (H1299) LUAD cells (Fig. S5D). We found that ZEB1
178 promoted secretory trafficking in the epithelial human (HCC827) LUAD cells and that the depletion
179 of REEP2 abated the phenotype (Fig. 5B). These findings suggest that REEP2 coordinates
180 ERES/Golgi colocalization to promote secretory trafficking.
181
182 **REEP2 regulates the secretion of pro-tumorigenic factors**

183 Given that REEP2 promotes secretory trafficking, we hypothesized that REEP2 facilitates the
184 secretion of pro-metastatic factors in mesenchymal LUAD cells. To test this, we evaluated
185 whether REEP2-dependent secretions could modulate epithelial LUAD cell behaviors in a
186 paracrine manner. Conditioned medium (CM) from REEP2-replete HCC827_ZEB1 cells induced
187 a decrease in the G_0/G_1 population and a corresponding increase in S-phase of HCC827_Vec
188 cells (Fig. 6A), and enhanced the cell mobility (Fig. 6B), whereas CM from REEP2-deficient
189 HCC827_ZEB1 cells demonstrated no effects (Fig. 6A and B). These findings suggest that the
190 REEP2-driven secretome contributes to the metastatic properties of LUAD cells.

191 To explore REEP2-dependent secreted factors, we performed liquid chromatography-mass
192 spectrometry (LC-MS) analysis on CM collected from REEP2-replete HCC827_ZEB1 cells, and
193 their REEP2-depleted counterparts. We found that REEP2 depletion reduced secretion of factors
194 involved in the immunomodulatory and cell migratory pathways (Fig. S6A, blue and red dots)
195 (Dataset S1), defined by enrichment analysis (Fisher's exact test using Gene Ontology terms) of
196 the down-regulated secreted proteins (Fig. S6B), including autotaxin (ATX). We have recently
197 identified ATX as a predominant secretory factor in the EMT-driven secretion that promotes LUAD
198 cell motility in autocrine and paracrine mechanisms and mediates the immunosuppressive TME
199 [11]. Enzyme-linked immunosorbent assays (ELISA) on CM samples confirmed that REEP2
200 depletion reduces the secretion of ATX (Fig. S6C), whereas the intracellular ATX remains
201 unchanged (Fig. S6D).

202 Given that we identified numerous immunomodulatory proteins that were diminished by
203 REEP2 depletion (Fig. S6A, red dots), we speculate that REEP2-regulated secretome remodels
204 TME. We used TIMER2.0 [39-41] to analyze the immune infiltrates in human LUAD cataloged in
205 TCGA. We found that high REEP2 expression positively correlates with higher infiltration levels
206 of myeloid-derived suppressor cells (MDSCs) and regulatory T cells (Tregs) in human LUAD (Fig.
207 6C and D). Therefore, we reasoned that REEP2 may create an immunosuppressive TME and
208 addressed this possibility by carrying out flow cytometry on flank tumors generated by REEP2-

209 replete or -deficient murine LUAD cells in syngeneic, immunocompetent mice. We found that
210 REEP2 depletion enhanced total $CD8^+$ T cells but reduced naïve $CD8^+$ T cells and MDSCs (Fig.
211 6E) in the TME, and suppressed tumor growth (Fig. 6F). These findings suggest that REEP2
212 promotes the secretion of pro-tumorigenic factors required for LUAD progression.
213
214 **Discussion**
215 Growing evidence shows that alterations in membrane trafficking frequently occur during
216 cancer progression and, in turn, promote metastasis [42], indicating significant therapeutic potential
217 for these pathways. Here, we show that EMT initiates a membrane trafficking program essential
218 for LUAD tumorigenesis under immunosurveillance and identify that ZEB1 coordinates REEP2
219 via miR-183/miR-193a to enhance ERES colocalization with the Golgi, thereby facilitating the
220 secretion of pro-metastatic factors that promote LUAD metastasis (Fig. 6G). This regulatory axis
221 discloses a potential therapeutic vulnerability in EMT-driven metastatic cancers.
222 The REEP family comprises six ER-localized membrane-shaping proteins that facilitate high
223 membrane curvature. REEP1-4 share structural motifs and are less abundant than REEP5 and
224 6, which are more broadly expressed [28]. Germline mutations in REEP1 and REEP2 cause
225 hereditary spastic paraplegia (HSP) and related motor neuropathies [43,44], underscoring their
226 physiological importance in ER shaping and neuronal maintenance. Additionally, REEP family
227 members have been implicated in tumor biology. REEP4 is upregulated in renal carcinoma, where
228 its expression aligns with tumor aggressiveness [45], and REEP6 expression correlates with poor
229 prognosis in oral squamous cell carcinoma [46]. Moreover, REEP5 and REEP6 have been shown
230 to potentiate CXCR1/IL-8 signaling and promote proliferation and metastasis in lung cancer cells
231 [47]. These findings suggest that REEP family proteins broadly contribute to tumor progression,
232 though their mechanisms and context-specific roles are still elusive. Here, we show for the first
233 time that REEP2 is a downstream effector of ZEB1-dependent transcription program that
234 activates ER-to-Golgi trafficking of secretory cargoes required for EMT-driven metastasis in LUAD.

235 A recent study demonstrated that REEP1-4 form a distinct ER-derived vesicular compartment
236 and regulate ER tubule dynamics [43,44], but their roles in membrane trafficking remain largely
237 unexplored. Here, we demonstrate that REEP2 is recruited to ERES, where it locates ERES on
238 the Golgi and, in turn, promotes secretory trafficking. Interestingly, although ectopic REEP2
239 expression is sufficient to drive ERES/Golgi colocalization in epithelial cells (Fig. 4E vs. Fig. 4C,
240 HCC827_Vec), REEP2 enhances the colocalization in a ZEB1-dependent manner (Fig. 4E).
241 Whether this occurs via direct interactions between REEP2 and its interactors, which are co-opted
242 by ZEB1, or indirectly through other altered membrane trafficking regulators in mesenchymal cells
243 warrants to be determined.
244 Here, we identified a set of REEP2-dependent secreted proteins. ATX is aberrantly secreted
245 by many human cancers to enhance cancer cell motility through lysophosphatidic acid receptors
246 (LPARs) [48-51]. Our recent study has shown that ATX is a key secretory effector within the EMT-
247 driven secretome, contributing to cell motility [11]. Furthermore, the ATX-CXCL1 axis recruits
248 MDSCs while inhibiting cytotoxic $CD8^+$ T-cell infiltration [52] and interleukin (IL)-6, a crucial regulator
249 of MDSC accumulation and activation [53]. REEP2 depletion suppresses the secretion of these
250 factors. These findings are consistent with clinical data and our mouse model, however, it remains
251 to be determined whether the REEP2-driven secretory program relates to LUAD progression and
252 metastasis and how it correlates to EMT and the immune landscape of the TME in LUAD patients.
253 In summary, our findings reveal REEP2 as a previously unrecognized effector of EMT-driven
254 membrane trafficking program in LUAD, highlighting that REEP2-mediated ERES-Golgi coupling
255 underlies the EMT-driven hypersecretory state.
256
257
258
259
260

261 **Methods**

262 Animal husbandry

263 For CRISPRi *in vivo* screen, all mouse studies were approved by the Institutional Animal Care
264 and Use Committee at The University of Texas MD Anderson Cancer Center (Houston, Texas).
265 Mice underwent standard care and were killed at predetermined time points or at first signs of
266 morbidity according to the standards set forth by the Institutional Animal Care and Use Committee.
267 To generate subcutaneous tumors, we injected 344SQ cells (1.1×10^6 cells in 100 μL PBS) into
268 the right flanks of syngeneic, immunocompetent 129-Elite (SOPF) mice (#476, Charles River
269 Laboratories) (n = 6 per cohort). Tumor volumes were monitored weekly until tumors reached
270 maximum size (~2 cm^3 total volume per mouse), and then the mice were sacrificed and the tumors
271 were harvested, as previously described [54].

272 All other mouse studies were approved by the Institutional Animal Care and Use Committee
273 at The University of Kentucky (Lexington, Kentucky). Mice underwent standard care and were
274 killed at predetermined time points or at first signs of morbidity according to the standards set
275 forth by the Institutional Animal Care and Use Committee. To generate orthotopic lung tumors,
276 we intrathoracically injected 344SQ cells (0.5×10^6 cells in 50 μL PBS) phosphate-buffered saline
277 into the left lungs of syngeneic, immunocompetent 129-Elite (SOPF) mice (n = 10 per cohort) and
278 carried out necropsies 14 d later to quantify primary tumor size and metastases to mediastinal
279 lymph nodes and contralateral lung as we previously described [11]. To generate subcutaneous
280 tumors, we injected 344SQ cells (0.5×10^6 cells in 100 μL PBS) into the right flanks of syngeneic,
281 immunocompetent 129-Elite (SOPF) mice (n = 10 per cohort). Tumor volumes were measured
282 weekly, and mice were sacrificed at 5 weeks post-injection, and necropsy was performed to
283 quantify primary tumor weights and assess the presence of pleural surface lung metastases, as
284 previously described [11].

285

286 CRISPRi screens

287 The CRISPRi library virus preparation and screen were performed as previously described [54]. In
288 brief, a library of gRNAs targeting 2,099 known or putatively membrane trafficking genes with 5
289 gRNAs per gene for a total of 11,040 gRNAs (#83992, Addgene) [27] in the pCRISPRia-v2 vector
290 (#84832, Addgene), and KRAB-dCas9-mCherry (#60954, Addgene), along with the psPax2
291 (Addgene cat# 12260) and pMD2.G (Addgene cat# 12259) lentiviral packaging vectors, were
292 transfected into 293T cells for virus production by The Functional Genomics Core (The University
293 of Texas MD Anderson Cancer Center, Houston, Texas). CRISPR library virus was used to titer
294 on the murine mesenchymal LUAD 344SQ cells. The amount of virus that resulted in ~30% cell
295 positivity following cell sorting selection based on the BFP signal in the pCRISPRia-v2 vector was
296 scaled up for library infection to ensure low multiplicity of infection (0.3) and appropriate library
297 representation (500X for each sgRNA) after selection. Cells were infected in triplicate to generate
298 biological replicates by The Functional Genomics Core.
299 On the day of animal injection, an initial time point (T0) of infected cells was harvested to
300 determine a baseline of sgRNA abundance. For *in vivo* CRISPRi screens, three independent
301 infections with the CRISPR library composed of biological replicates in the screening experiments.
302 Each replicate was inoculated into the right flanks of 6 different 6-8-week-old 129-Elite (SOPF)
303 mice with 1.1 million cells per injection. The tumors were harvested when they reached ~2 cm^3
304 total volume. The T0 infected cells and tumors were digested and the genomic DNA was extracted
305 by The Biospecimen Extraction Facility (The University of Texas MD Anderson Cancer Center,
306 Houston, Texas). The next-generation sequencing of sgRNA and analysis of sgRNA abundance
307 were performed by VectorBuilder Inc. (Chicago, Illinois).
308
309 Reagents
310 We purchased fetal bovine serum (FBS), live-cell imaging solution, phosphate-buffered saline
311 (PBS), RPMI-1640, Trypsin-EDTA (0.25%), Alexa Fluor-tagged secondary antibodies,
312 paraformaldehyde, bovine serum albumin (BSA), DAPI and Triton X-100, High-Capacity cDNA

313 Reverse Transcription Kit, PowerUp™ SYBR™ Green Master Mix, and protease/phosphatase
314 inhibitor cocktail from Thermo Fisher Scientific; Doxycycline (#D9891) from MilliporeSigma;
315 Bronchial Epithelial Cell Growth Medium BulletKit from Lonza; jetPRIME transfection reagent from
316 Polyplus Transfection; Transwell and Matrigel-coated Boyden chambers from BD Biosciences;
317 Glass-bottom dishes and multiwell plates from MatTek; 10X Cell lysis buffer from Cell Signaling
318 Technologies; 2X cell lysis buffer (#1610737) from Bio-Rad; CCK-8 (#K1018) from APExBIO;
319 RNeasy Plus Mini Kit (#74136), and AllStars Negative Control siRNA (#1027281) from QIAGEN;
320 Pre-miR™ miRNA Precursor Negative Control (miR-NC) (#AM17110); human miR-183a mimics
321 (#PM12303) and human miR-193 mimics (#PM11786) from Thermo Fisher Scientific; human
322 REEP2 siRNA #2 (#J-021201-18), and #4 (J-021201-20) from Horizon; primary antibodies against
323 β-actin (#4967), ZEB1 (#3396) from Cell Signaling Technologies, REEP2 (#Ab191410) from
324 Abcam, SEC16A (#20025-1-AP) from Proteintech, VSV-G (#EB0012) from Kerafast; Alexa Fluor
325 555 Mouse anti-GM130 (#560066) from BD Biosciences; REEP2-GFP (#RC202507L4) from
326 Origene; SEC24D-mCherry (#32677), Golgi-pmTurquoise2 (#36205), mCherry-Golgi (#55052)
327 and CD-MPR-GFP-RUSH (#202797) from Addgene; 3'-UTR luciferase reporters of REEP2
328 (#38786081) from Applied Biological Materials; pCI-Neo Renilla luciferase reporter (Basic)
329 (#E1841) and pGL3 Basic Firefly luciferase control reporter (#E1751) from Promega; All-in-One
330 miRNA qRT-PCR Detection Kit 2.0 (#QP115) from GeneCopoeia.
331
332 Cell lines and culture
333 Murine LUAD cell lines were derived previously [26]. Human LUAD cell lines were from Jonathan
334 Kurie (The University of Texas MD Anderson Cancer Center, Houston, Texas). Human
335 HBEC30KT cell line was from John Minna (The University of Texas Southwestern Medical Center,
336 Dallas, Texas). Murine and human LUAD cell lines were cultured in RPMI-1640 with 10% FBS.
337 Human HBEC30KT cell line was cultured in Bronchial Epithelial Cell Growth Medium BulletKit.

338 Cells were maintained at 37°C in an incubator with a humidified atmosphere containing 5% CO2.
339 Cells were transfected with vectors using jetPRIME transfection reagent.
340
341 CRISPR/Cas9
342 CRISPR-Cas9-mediated murine REEP2 Knockout 344SQ cells were generated in the Cell-Based
343 Assay Screening Service Core Facility (Baylor College of Medicine) using the following guide
344 RNA sequences: 5′-aaagaugagccuagggaagc-3' and 5′-aaacagaugggaguagagug-3'.
345
346 Live and fixed cell imaging
347 Cells were seeded on type I collagen-coated cover glass (#1.5). Live cells were imaged in live-
348 cell imaging media within incubation chambers. For fixed-cell imaging, cells were fixed using 4%
349 paraformaldehyde for 10 min, permeabilized using 0.1% Triton X-100 for 5 min, and blocked with
350 5% BSA for 1h. Primary antibody incubation was performed in blocking buffer for 1 h overnight at
351 4°C, followed by Alexa Fluor-conjugated secondary antibodies in blocking buffer for 1 h at room
352 temperature. Nuclei were counterstained with DAPI (#R37606, Thermo Fisher Scientific), and a
353 cover glass was mounted using ProLong Diamond Antifade Mountant (#P36970, Thermo Fisher
354 Scientific). Each step was followed by washing 3 times with PBS, which was also used as the
355 solvent in all steps. For VSV-G assay, the cells were not permeabilized.
356
357 VSV-G assay
358 The VSV-G transport assay was performed as described previously [11]. In brief, cells were
359 transiently transfected with EGFP-VSV-G (ts045), transferred to the restrictive temperature of
360 40°C for 20 h, and then transferred to the permissive temperature of 32°C for 1 h in the presence
361 of 100 mg/ml cycloheximide, at which point the cells were fixed. In nonpermeabilized cells,
362 exofacial and total VSV-G were detected by staining with an anti–VSV-G antibody and by
363 measurement of EGFP signal intensity, respectively. VSV-G trafficking to the plasma membrane

364 was measured based on the ratio of exofacial (surface) VSV-G fluorescence signal to the EGFP
365 (total) signal intensity.
366
367 RUSH assay
368 The RUSH assay was performed as described previously [37,55]. In brief, cells were transiently
369 transfected with a CD-MPR reporter, which is fused to the streptavidin-binding peptide (SBP),
370 GFP-tag, and a second protein with a C-terminal ER retention signal (Lys-Asp-Glu-Leu; KDEL)
371 fusing with streptavidin as a hook (#202797, Addgene). mCherry-Golgi (#55052, Addgene) was
372 transiently co-transfected to label the Golgi compartment. BioLock (#2-0205-050, IBA Life
373 Sciences) was used to quench excessive biotin in the culture medium according to manufacturer's
374 instructions. Twenty hours after transfection, the release of the RUSH cargos was induced by
375 addition of 40 μM of D-biotin (#B4501, MilliporeSigma). Time-lapse acquisitions were done at 37
376 °C in a thermostat-controlled Nikon stage top incubator (Nikon Instruments).
377
378 Microscopy
379 Fixed and live-cell imaging were performed on Nikon CSU-W1 SoRa Confocal Microscope (Nikon
380 Instruments) equipped with 60X/1.4 NA Oil, 100X/1.45 NA Oil objectives; 405/488/561/647 nm
381 laser lines; GaAsP detectors, and Nikon stage top incubator. Images were acquired using NIS-
382 Elements software (Nikon instruments).
383
384 Image processing and quantitative analysis
385 For fixed cell imaging, the raw images were processed, and fluorescent intensity was analyzed in
386 Fiji/ImageJ (www.imagej.nih.gov). For live cell imaging, the raw images were processed/analyzed
387 in Imaris 10.0.1 (Bitplane software, Oxford instruments) with Spot features and MATLAB
388 XTensions.
389

390 Quantitative RT-PCR

391 Total RNA was isolated from cells using RNeasy Plus Mini Kit and subjected to reverse
392 transcription and qPCR analysis as described [56]. mRNA levels were normalized based on
393 ribosomal protein L32 (RPL32) mRNA. MicroRNA levels were detected using the All-in-One
394 miRNA qRT-PCR Detection Kit 2.0 with a universal reverse primer (#QP115, GeneCopoeia)
395 according to the manufacturer's instructions and normalized to U6. Primer sequences are listed
396 in Table S3.

397

398 Luciferase reporter assays

399 For 3′-UTR activity assays, H1299 cells were co-transfected with luciferase reporters driven by
400 REEP2-3'-UTR sequences (100 ng) or pCI-Neo Renilla luciferase reporter (Basic) (100 ng), pGL3
401 Basic Firefly luciferase control reporter (100 ng), and microRNA mimics or control mimics (20 μM).
402 After 48 hours, firefly and Renilla luciferase activities were measured with the Dual-Luciferase
403 Reporter Assay System (Promega).

404

405 Mutagenesis

406 Q5 Site-Directed Mutagenesis Kit (#E0554S, NEB) was used to generate mutants according to
407 the manufacturer's instructions. The primer sequences utilized for mutagenesis are: 5'-
408 TCATTGGGTGGGGCTGAAAAAAACATGTTCCCACATTAAAA-3' and 5'-
409 CAGCCCCACCCAATGACCAGGAAAAGAG-3' for human REEP2 3'UTR MT1 (miR-183 binding
410 stie); 5′-AAAGAGGCCCCTCCTGAGGCTTCA-3′ and 5′-TTTAGCCCCTGCTCCACACTGTGC-3′
411 for human REEP2 3'UTR MT2 (miR-193a binding stie 1); 5′-
412 AAATAGGGCCCAGTCTGCTTGGTACAG-3′ and 5′-TTTTCTGGCAGAACCCAGCCTCTG-3′ for
413 human REEP2 3'UTR MT3 (miR-193a binding stie 2). All primers were purchased from Integrated
414 DNA Technologies.

415

416 Western blotting

417 Cells cultured in each well of a 6-well plate at 80% confluency were washed three times with PBS
418 and harvested/resuspended in 150–200 μl of 2× Laemmli buffer (Bio-Rad). The cell lysate was
419 boiled for 10 min and loaded onto an SDS gel. After transferring to a nitrocellulose membrane
420 (Bio-Rad), membranes were blocked with 5% milk in TBST buffer and were probed with primary
421 antibodies diluted in 5% BSA in TBST buffer. Horseradish peroxidase (HRP)-conjugated
422 secondary antibodies were used according to the manufacturers' instructions. Quantitative
423 analysis was performed by using Fiji/ImageJ (NIH).

424

425 Cell proliferation assay

426 Cells were seeded on 96-well plates at a density of $2*10^3$ cells per well on day 0. Relative cell
427 density was measured by using the CCK-8 Counting Kit according to the manufacturer's
428 instructions. Briefly, cells were incubated with culture medium containing the CCK-8 solution for
429 2 h at 37 °C, and the absorbance was read at 450 nm.

430

431 Cell cycle assay

432 Cells were synchronized using culture medium containing 0.1% FBS for 24 h, then allowed to
433 grow in culture medium containing 10% FBS for 24 h. The cells were fixed with 70% ethanol at
434 4°C overnight, and were incubated with Propidium Iodide (PI)/RNase Staining Solution (#4087S,
435 Cell Signaling Technologies) for 30 min. After incubation, cell cycle was analyzed using a flow
436 cytometer (BD Symphony).

437

438 Cell apoptosis assay

439 Cells were harvested and then incubated with 7-AAD (#420404, BioLegend) and Annexin-V
440 (#640926, BioLegend) at room temperature for 10-20 min. After incubation, cell apoptosis was
441 analyzed using a flow cytometer (BD Symphony).

442

443 Cell migration and invasion assays in Boyden chambers

444 As described previously [11], $1*10^5$ cells were seeded in the upper wells of Transwell for migration
445 and Matrigel-coated Boyden chambers for invasion assays, respectively (BD Biosciences) and
446 allowed to migrate toward 10% FBS in the bottom wells. After 16 h of incubation, migrating or
447 invading cells were stained with 0.1% crystal violet, photographed, and counted. For conditioned
448 medium (CM) transfer experiments, CM samples were isolated, filtered through a 0.45-μm filter,
449 and applied to cells seeded in the upper wells.

450

451 Liquid chromatography/mass spectrometry (LC-MS)

452 The immunoprecipitation (IP) from agarose beads was then washed with ice-cold lysis buffer 5
453 times. The bound proteins on beads were eluted in 5% SDS. For mass spectrometry analysis,
454 samples were reduced, alkylated, and digested using trypsin on an S-trap as described [57]. The
455 resultant peptides were quantified and normalized within sets by the Quantitative Fluorometric
456 Peptide Assay. Samples were analyzed using a 90-minute gradient on our Orbitrap Eclipse. The
457 resulting Liquid chromatography-mass spectrometry (LC-MS) data was processed in Proteome
458 Discoverer 2.5 and SEQUEST using a human database. The minora node was used to perform
459 Label-Free Quantitation (LFQ) using the MS peak areas for each of the peptide-spectral matches.
460 The IP-MS was performed in triplicate.

461

462 Immune cell profiling

463 Mouse flank tumors generated by subcutaneous injection of $0.5*10^6$ parental 344SQ or
464 344SQ_REEP2_KO #25 or #44 cells into the flank of wild-type mice for 5 weeks were harvested.
465 The tumor tissues and mouse spleens were processed for isolating tumor-infiltrating lymphocytes
466 by The Flow Cytometry and Immune Monitoring Core Facility (University of Kentucky, Lexington,
467 Kentucky). Single-cell suspension was stained as described previously [11] with the following

468 antibodies: CD3-PE-594 (#100246, BioLegend), CD45-Pacific Blue (#103126, BioLegend), CD4-
469 APCCy7 (#100526, BioLegend), CD8-PE-Cy7 (#100721, BioLegend), CD278-PE (#117406,
470 BioLegend), CD25-BUV395 (#564022, BD Biosciences), PD1-BV-505 (#135220, BioLegend),
471 CD62L-FITC (#35-0621-U500, Thermo Fisher Scientific), CD44-BV-711 (#103057, BioLegend),
472 TIM3-APC (#134007, BioLegend), FoxP3-PerCP-Cy5.5 (#45-5773-82, Invitrogen), GR1-BV-711
473 (#106443, BioLegend), CD11b-BV-650 (#101239, BioLegend), CD11c-BV-785 (#117335,
474 BioLegend), F4/80-APC (#204801-U100, Tonbo), PDL1-PE-Dazzle-594 (#124323, BioLegend),
475 CD86-APC-Cy7 (#105030, BioLegend), MCHII-PE-Cy7 (#107629, BioLegend), CD80-BV-605
476 (#104729, BioLegend), CD68-PerCP-Cy5.5 (#137009, BioLegend), iNOS-PE (#125920-80,
477 Invitrogen), Arg1-FITC (IC5868F, R&D Systems), CD31-BV-786 (#740870, BD Biosciences), and
478 the live/dead cell marker Ghost Violet-BV-510 (#10-0870-T100, VWR). For intracellular staining,
479 cells were fixed and permeabilized using the intracellular staining perm wash buffer (BioLegend)
480 according to manufacturer instructions. Data were acquired using a flow cytometer (BD
481 Symphony) and analyzed using FlowJo software (version 10.10.0; BD Biosciences).
482
483 Analysis of Kaplan-Meier Survival Data
484 LUAD patient survival data were downloaded from the Kaplan-Meier plotter database [58]. Analysis
485 of LUAD patients was performed in REEP2 high- and low-expression cohorts. The *P* value was
486 calculated using the log-rank test [58].
487
488 TNMplot analysis
489 The REEP2 mRNA expression analysis in normal lung and different stages of lung tumor tissues
490 was performed as previously described [59].
491
492 Statistical analysis

493 Unless mentioned otherwise, the results shown are representative of replicated experiments and
494 are the means ± standard error of the means (SEM) from triplicate samples or randomly chosen
495 cells within a field. The comparison of mRNA levels with EMT scores and the correlation analysis
496 in human lung cancers were performed as previously described [60], and the EMT score was
497 calculated as previously described [60,61]. Statistical evaluations were carried out with Prism 9
498 (GraphPad Software, Inc.). Unpaired 2-tailed Student t-tests or ANOVA were used to compare
499 means for two or more groups, respectively, and P values < 0.05 were considered statistically
500 significant.
501
502

503 **Data, materials, and software availability**

504 All data are available in the main text or the supporting information.

505

506 **Acknowledgement**

507 This work was supported by the National Institutes of Health (NIH) through R00 CA249048 (to
508 G.X.), R03 CA280382 (to X.T.), R01 CA181184 (to J.M.K.), R01 CA2111125 (to J.M.K.), NIH
509 Lung Cancer SPORE grant P50 CA70907 (to J.M.K.). We thank The Functional Genomics Core
510 (The University of Texas MD Anderson Cancer Center) for CRISPRi library virus preparation and
511 cell infection, and The Biospecimen Extraction Facility (The University of Texas MD Anderson
512 Cancer Center) for genomic DNA extraction from CRISPRi in vivo screen. This research was
513 supported by the Flow Cytometry and Immune Monitoring (FCIM) Shared Resource of the
514 University of Kentucky Markey Cancer Center (P30CA177558). We thank the FCIM for tumor
515 tissue processing for immune cell profiling.

516

517 **Author contributions**

518 K.F., O.O., and G.X. conceived, designed, executed, and interpreted all experiments. S.W. and
519 X.T. assisted with mutagenesis for 3'-UTR reporter assays. X.L. and J.Y. assisted with mouse
520 experiments for CRISPRi *in vivo* screen. J.M.K. supported and supervised the CRISPRi *in vivo*
521 screen. J.X. assisted with CRISPR/Cas9-mediated genome-editing cell line establishment. W.K.R.
522 directed and interpreted mass spectrometry experiments. X.T. and G.X. supervised the project
523 and contributed to the design and interpretation of all experiments.

524

525 **Competing Interest Statement:** J.M.K. has received consulting fees from Halozyme. All other
526 authors declare that they have no competing interests.

527

528

References

1 Tan, X., Xiao, G. Y., Banerjee, P., Wang, S. & Kurie, J. M. The cancer-associated secretory phenotype: a new frontier in targeted therapeutics. *J Clin Invest* **134**, doi:10.1172/JCI182652 (2024).

2 Ferreira, A., Castanheira, P., Escrevente, C., Barral, D. C. & Barona, T. Membrane trafficking alterations in breast cancer progression. *Front Cell Dev Biol* **12**, 1350097, doi:10.3389/fcell.2024.1350097 (2024).

3 Tejeda-Munoz, N., Mei, K. C., Sheladiya, P. & Monka, J. Targeting Membrane Trafficking as a Strategy for Cancer Treatment. *Vaccines (Basel)* **10**, doi:10.3390/vaccines10050790 (2022).

4 Huang, D. *et al.* Up-regulated ADP-Ribosylation factor 3 promotes breast cancer cell proliferation through the participation of FOXO1. *Exp Cell Res* **384**, 111624, doi:10.1016/j.yexcr.2019.111624 (2019).

5 Makaraci, P. & Kim, K. trans-Golgi network-bound cargo traffic. *Eur J Cell Biol* **97**, 137-149, doi:10.1016/j.ejcb.2018.01.003 (2018).

6 Elkin, S. R., Lakoduk, A. M. & Schmid, S. L. Endocytic pathways and endosomal trafficking: a primer. *Wien Med Wochenschr* **166**, 196-204, doi:10.1007/s10354-016-0432-7 (2016).

7 Maxfield, F. R. & McGraw, T. E. Endocytic recycling. *Nat Rev Mol Cell Biol* **5**, 121-132, doi:10.1038/nrm1315 (2004).

8 Di Martino, R., Sticco, L. & Luini, A. Regulation of cargo export and sorting at the trans-Golgi network. *FEBS Lett* **593**, 2306-2318, doi:10.1002/1873-3468.13572 (2019).

9 Mosesson, Y., Mills, G. B. & Yarden, Y. Derailed endocytosis: an emerging feature of cancer. *Nat Rev Cancer* **8**, 835-850, doi:10.1038/nrc2521 (2008).

10 Lanzetti, L. & Di Fiore, P. P. Endocytosis and cancer: an 'insider' network with dangerous liaisons. *Traffic* **9**, 2011-2021, doi:10.1111/j.1600-0854.2008.00816.x (2008).

11 Xiao, G. Y. *et al.* EMT activates exocytotic Rabs to coordinate invasion and immunosuppression in lung cancer. *Proc Natl Acad Sci U S A* **120**, e2220276120, doi:10.1073/pnas.2220276120 (2023).

12 Tan, X. *et al.* EMT-activated secretory and endocytic vesicular trafficking programs underlie a vulnerability to PI4K2A antagonism in lung cancer. *J Clin Invest* **133**, doi:10.1172/JCI165863 (2023).

13 Tan, X. *et al.* p53 loss activates prometastatic secretory vesicle biogenesis in the Golgi. *Sci Adv* **7**, doi:10.1126/sciadv.abf4885 (2021).

14 Banerjee, P. *et al.* The EMT activator ZEB1 accelerates endosomal trafficking to establish a polarity axis in lung adenocarcinoma cells. *Nat Commun* **12**, 6354, doi:10.1038/s41467-021-26677-y (2021).

15 Xiao, G. Y. & Schmid, S. L. FCHSD2 controls oncogenic ERK1/2 signaling outcome by regulating endocytic trafficking. *PLoS Biol* **18**, e3000778, doi:10.1371/journal.pbio.3000778 (2020).

16 Lakoduk, A. M. *et al.* Mutant p53 amplifies a dynamin-1/APPL1 endosome feedback loop that regulates recycling and migration. *J Cell Biol* **218**, 1928-1942, doi:10.1083/jcb.201810183 (2019).

17 Xiao, G. Y., Mohanakrishnan, A. & Schmid, S. L. Role for ERK1/2-dependent activation of FCHSD2 in cancer cell-selective regulation of clathrin-mediated endocytosis. *Proc Natl Acad Sci U S A* **115**, E9570-E9579, doi:10.1073/pnas.1810209115 (2018).

18 Schmid, S. L. Reciprocal regulation of signaling and endocytosis: Implications for the evolving cancer cell. *J Cell Biol* **216**, 2623-2632, doi:10.1083/jcb.201705017 (2017).

19 Chen, P. H. *et al.* Crosstalk between CLCb/Dyn1-Mediated Adaptive Clathrin-Mediated Endocytosis and Epidermal Growth Factor Receptor Signaling Increases Metastasis. *Dev Cell* **40**, 278-288 e275, doi:10.1016/j.devcel.2017.01.007 (2017).
20 Reis, C. R. *et al.* Crosstalk between Akt/GSK3beta signaling and dynamin-1 regulates clathrin-mediated endocytosis. *EMBO J* **34**, 2132-2146, doi:10.15252/embj.201591518 (2015).
21 Liberali, P., Snijder, B. & Pelkmans, L. A hierarchical map of regulatory genetic interactions in membrane trafficking. *Cell* **157**, 1473-1487, doi:10.1016/j.cell.2014.04.029 (2014).
22 Pelkmans, L. *et al.* Genome-wide analysis of human kinases in clathrin- and caveolae/raft-mediated endocytosis. *Nature* **436**, 78-86, doi:10.1038/nature03571 (2005).
23 Corallino, S., Malabarba, M. G., Zobel, M., Di Fiore, P. P. & Scita, G. Epithelial-to-Mesenchymal Plasticity Harnesses Endocytic Circuitries. *Front Oncol* **5**, 45, doi:10.3389/fonc.2015.00045 (2015).
24 Tan, X. *et al.* Epithelial-to-mesenchymal transition drives a pro-metastatic Golgi compaction process through scaffolding protein PAQR11. *J Clin Invest* **127**, 117-131, doi:10.1172/JCI88736 (2017).
25 Ahn, Y. H. *et al.* ZEB1 drives prometastatic actin cytoskeletal remodeling by downregulating miR-34a expression. *J Clin Invest* **122**, 3170-3183, doi:10.1172/JCI63608 (2012).
26 Gibbons, D. L. *et al.* Contextual extracellular cues promote tumor cell EMT and metastasis by regulating miR-200 family expression. *Genes Dev* **23**, 2140-2151, doi:10.1101/gad.1820209 (2009).
27 Horlbeck, M. A. *et al.* Compact and highly active next-generation libraries for CRISPR-mediated gene repression and activation. *Elife* **5**, doi:10.7554/eLife.19760 (2016).
28 Fan, S., Liu, H. & Li, L. The REEP family of proteins: Molecular targets and role in pathophysiology. *Pharmacol Res* **185**, 106477, doi:10.1016/j.phrs.2022.106477 (2022).
29 Hurt, C. M. *et al.* REEP1 and REEP2 proteins are preferentially expressed in neuronal and neuronal-like exocytotic tissues. *Brain Res* **1545**, 12-22, doi:10.1016/j.brainres.2013.12.008 (2014).
30 Weigel, A. V. *et al.* ER-to-Golgi protein delivery through an interwoven, tubular network extending from ER. *Cell* **184**, 2412-2429 e2416, doi:10.1016/j.cell.2021.03.035 (2021).
31 Szul, T. & Sztul, E. COPII and COPI traffic at the ER-Golgi interface. *Physiology (Bethesda)* **26**, 348-364, doi:10.1152/physiol.00017.2011 (2011).
32 Robinson, C. M., Duggan, A. & Forrester, A. ER exit in physiology and disease. *Front Mol Biosci* **11**, 1352970, doi:10.3389/fmolb.2024.1352970 (2024).
33 Sprangers, J. & Rabouille, C. SEC16 in COPII coat dynamics at ER exit sites. *Biochem Soc Trans* **43**, 97-103, doi:10.1042/BST20140283 (2015).
34 Hughes, H. *et al.* Organisation of human ER-exit sites: requirements for the localisation of Sec16 to transitional ER. *J Cell Sci* **122**, 2924-2934, doi:10.1242/jcs.044032 (2009).
35 Linstedt, A. D. *et al.* Binding relationships of membrane tethering components. The giantin N terminus and the GM130 N terminus compete for binding to the p115 C terminus. *J Biol Chem* **275**, 10196-10201, doi:10.1074/jbc.275.14.10196 (2000).
36 Shibata, Y. *et al.* The membrane curvature-inducing REEP1-4 proteins generate an ER-derived vesicular compartment. *Nat Commun* **15**, 8655, doi:10.1038/s41467-024-52901-6 (2024).
37 Boncompain, G. *et al.* Synchronization of secretory protein traffic in populations of cells. *Nat Methods* **9**, 493-498, doi:10.1038/nmeth.1928 (2012).
38 Waguri, S. *et al.* Visualization of TGN to endosome trafficking through fluorescently labeled MPR and AP-1 in living cells. *Mol Biol Cell* **14**, 142-155, doi:10.1091/mbc.e02-06-0338 (2003).

39 Li, T. *et al.* TIMER2.0 for analysis of tumor-infiltrating immune cells. *Nucleic Acids Res* **48**, W509-W514, doi:10.1093/nar/gkaa407 (2020).
40 Li, T. *et al.* TIMER: A Web Server for Comprehensive Analysis of Tumor-Infiltrating Immune Cells. *Cancer Res* **77**, e108-e110, doi:10.1158/0008-5472.CAN-17-0307 (2017).
41 Li, B. *et al.* Comprehensive analyses of tumor immunity: implications for cancer immunotherapy. *Genome Biol* **17**, 174, doi:10.1186/s13059-016-1028-7 (2016).
42 Evergren, E., Mills, I. G. & Kennedy, G. Adaptations of membrane trafficking in cancer and tumorigenesis. *J Cell Sci* **137**, doi:10.1242/jcs.260943 (2024).
43 Zuchner, S. *et al.* Mutations in the novel mitochondrial protein REEP1 cause hereditary spastic paraplegia type 31. *Am J Hum Genet* **79**, 365-369, doi:10.1086/505361 (2006).
44 Esteves, T. *et al.* Loss of association of REEP2 with membranes leads to hereditary spastic paraplegia. *Am J Hum Genet* **94**, 268-277, doi:10.1016/j.ajhg.2013.12.005 (2014).
45 Chen, Z., Jia, X. & Liu, M. REEP4 as Potential Biomarker Associated with Predictive Prognosis and Immune Response in Kidney Clear Cell Carcinoma. *J Cancer* **15**, 4143-4155, doi:10.7150/jca.96135 (2024).
46 Tseng, C. C. *et al.* The Clinical and Biological Effects of Receptor Expression-Enhancing Protein 6 in Tongue Squamous Cell Carcinoma. *Biomedicines* **11**, doi:10.3390/biomedicines11051270 (2023).
47 Park, C. R. *et al.* The accessory proteins REEP5 and REEP6 refine CXCR1-mediated cellular responses and lung cancer progression. *Sci Rep* **6**, 39041, doi:10.1038/srep39041 (2016).
48 Liu, S., Murph, M., Panupinthu, N. & Mills, G. B. ATX-LPA receptor axis in inflammation and cancer. *Cell Cycle* **8**, 3695-3701, doi:10.4161/cc.8.22.9937 (2009).
49 Aiello, S. & Casiraghi, F. Lysophosphatidic Acid: Promoter of Cancer Progression and of Tumor Microenvironment Development. A Promising Target for Anticancer Therapies? *Cells* **10**, doi:10.3390/cells10061390 (2021).
50 Kato, K. *et al.* Opposite roles of LPA1 and LPA3 on cell motile and invasive activities of pancreatic cancer cells. *Tumour Biol* **33**, 1739-1744, doi:10.1007/s13277-012-0433-0 (2012).
51 Yu, S. *et al.* Lysophosphatidic acid receptors determine tumorigenicity and aggressiveness of ovarian cancer cells. *J Natl Cancer Inst* **100**, 1630-1642, doi:10.1093/jnci/djn378 (2008).
52 Pietrobono, S. *et al.* Autotaxin Secretion Is a Stromal Mechanism of Adaptive Resistance to TGFbeta Inhibition in Pancreatic Ductal Adenocarcinoma. *Cancer Res* **84**, 118-132, doi:10.1158/0008-5472.CAN-23-0104 (2024).
53 Weber, R. *et al.* IL-6 as a major regulator of MDSC activity and possible target for cancer immunotherapy. *Cell Immunol* **359**, 104254, doi:10.1016/j.cellimm.2020.104254 (2021).
54 Martin, T. D. *et al.* The adaptive immune system is a major driver of selection for tumor suppressor gene inactivation. *Science* **373**, 1327-1335, doi:10.1126/science.abg5784 (2021).
55 Boncompain, G. & Perez, F. Synchronizing protein transport in the secretory pathway. *Curr Protoc Cell Biol* **Chapter 15**, 15 19 11-15 19 16, doi:10.1002/0471143030.cb1519s57 (2012).
56 Tan, X. *et al.* The epithelial-to-mesenchymal transition activator ZEB1 initiates a prometastatic competing endogenous RNA network. *J Clin Invest* **128**, 1267-1282, doi:10.1172/JCI97225 (2018).
57 Mascibroda, L. G. *et al.* INTS13 variants causing a recessive developmental ciliopathy disrupt assembly of the Integrator complex. *Nat Commun* **13**, 6054, doi:10.1038/s41467-022-33547-8 (2022).

58 Gyorffy, B., Surowiak, P., Budczies, J. & Lanczky, A. Online survival analysis software to assess the prognostic value of biomarkers using transcriptomic data in non-small-cell lung cancer. *PLoS One* **8**, e82241, doi:10.1371/journal.pone.0082241 (2013).

59 Bartha, A. & Gyorffy, B. TNMplot.com: A Web Tool for the Comparison of Gene Expression in Normal, Tumor and Metastatic Tissues. *Int J Mol Sci* **22**, doi:10.3390/ijms22052622 (2021).

60 Gibbons, D. L. & Creighton, C. J. Pan-cancer survey of epithelial-mesenchymal transition markers across the Cancer Genome Atlas. *Dev Dyn* **247**, 555-564, doi:10.1002/dvdy.24485 (2018).

61 Byers, L. A. *et al.* An epithelial-mesenchymal transition gene signature predicts resistance to EGFR and PI3K inhibitors and identifies Axl as a therapeutic target for overcoming EGFR inhibitor resistance. *Clin Cancer Res* **19**, 279-290, doi:10.1158/1078-0432.CCR-12-1558 (2013).

Figures

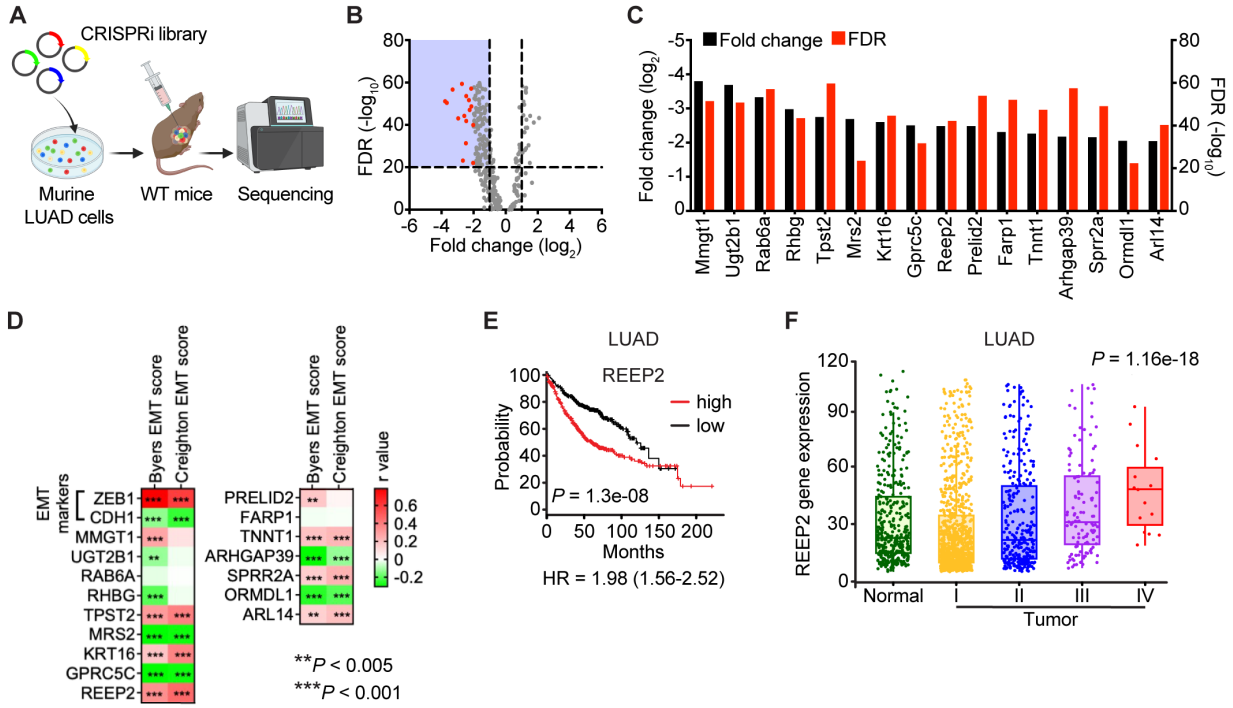

Figure 1. Pro-tumorigenic membrane trafficking program for LUAD growth. (A) A CRISPRi library targeting membrane trafficking genes was transduced into 344SQ murine LUAD cells. Cells were transplanted subcutaneously on the flanks of WT syngeneic mice. Following tumor formation, the tumors were harvested and sgRNAs were sequenced. (B) Volcano plots of the analyses of the screening results in immunocompetent WT mice. Grey dots represent membrane trafficking genes, and vertical and horizontal dotted lines indicate fold-change ($\log_2$) = ±1 and FDR ($-\log_{10}$) = 20, respectively. The red dots represent the top hits that fold-change ($\log_2$) < -2 and FDR ($-\log_{10}$) > 20. (C) The bar graph represents the top hits in (B) (Red dots). (D) Heat map illustration of correlation between mRNA levels of indicated genes and EMT scores (Byers or Creighton) in the TCGA LUAD cohort. r values: Pearson correlation. (E) Kaplan-Meier survival analysis of LUAD patients based on REEP2 mRNA levels above (high) or below (low) the median value. (F) Expression levels of REEP2 mRNA in normal lung tissues (n = 391), stage I (n = 905), stage II (n = 331), stage III (n = 146), and stage IV lung tumors (n = 17) using data from TNMplot. (https://tnmplot.com/).

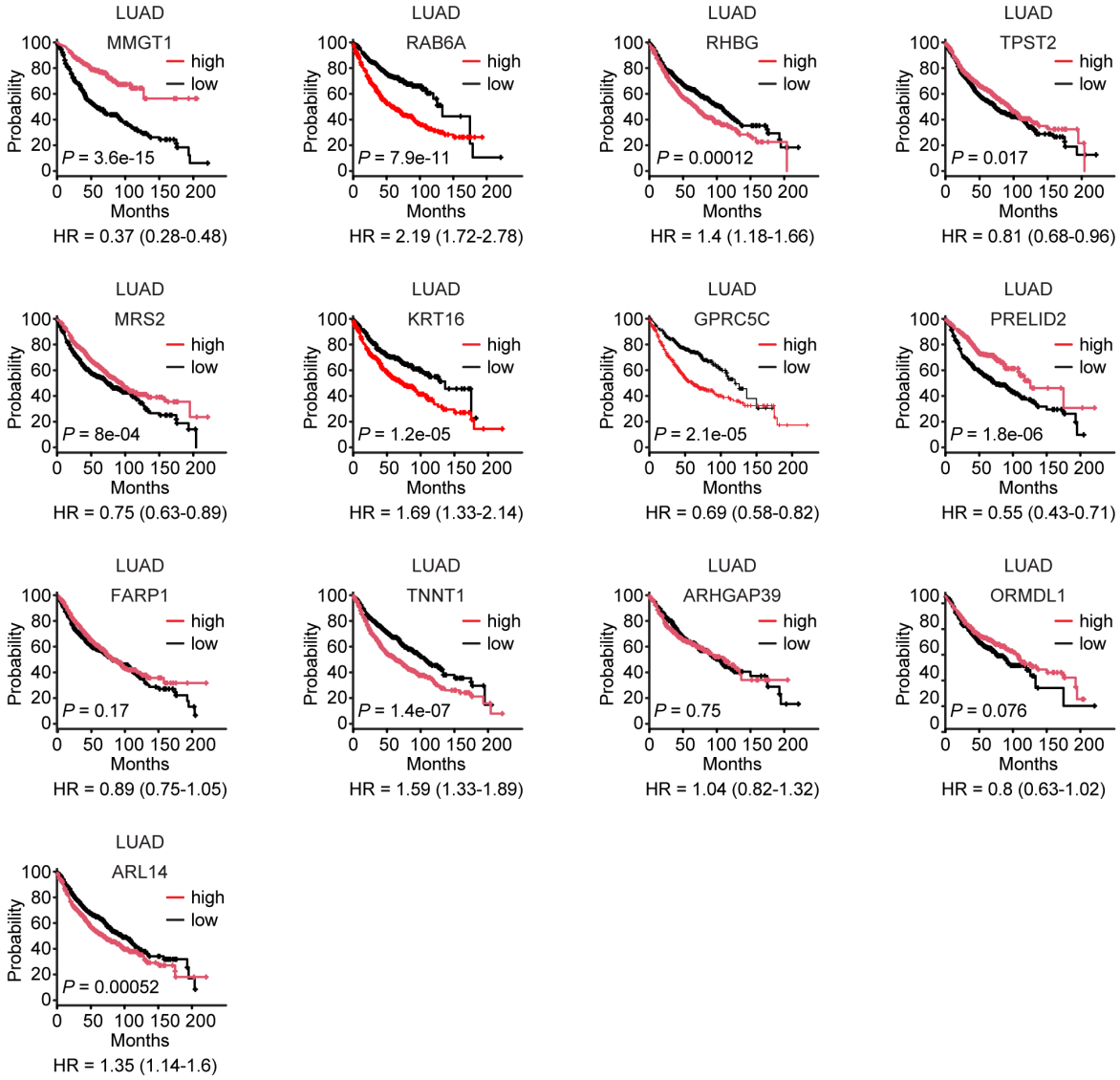

Fig. S1. Kaplan-Meier survival analysis of LUAD patients based on the mRNA levels of indicated genes above (high) or below (low) the median value.

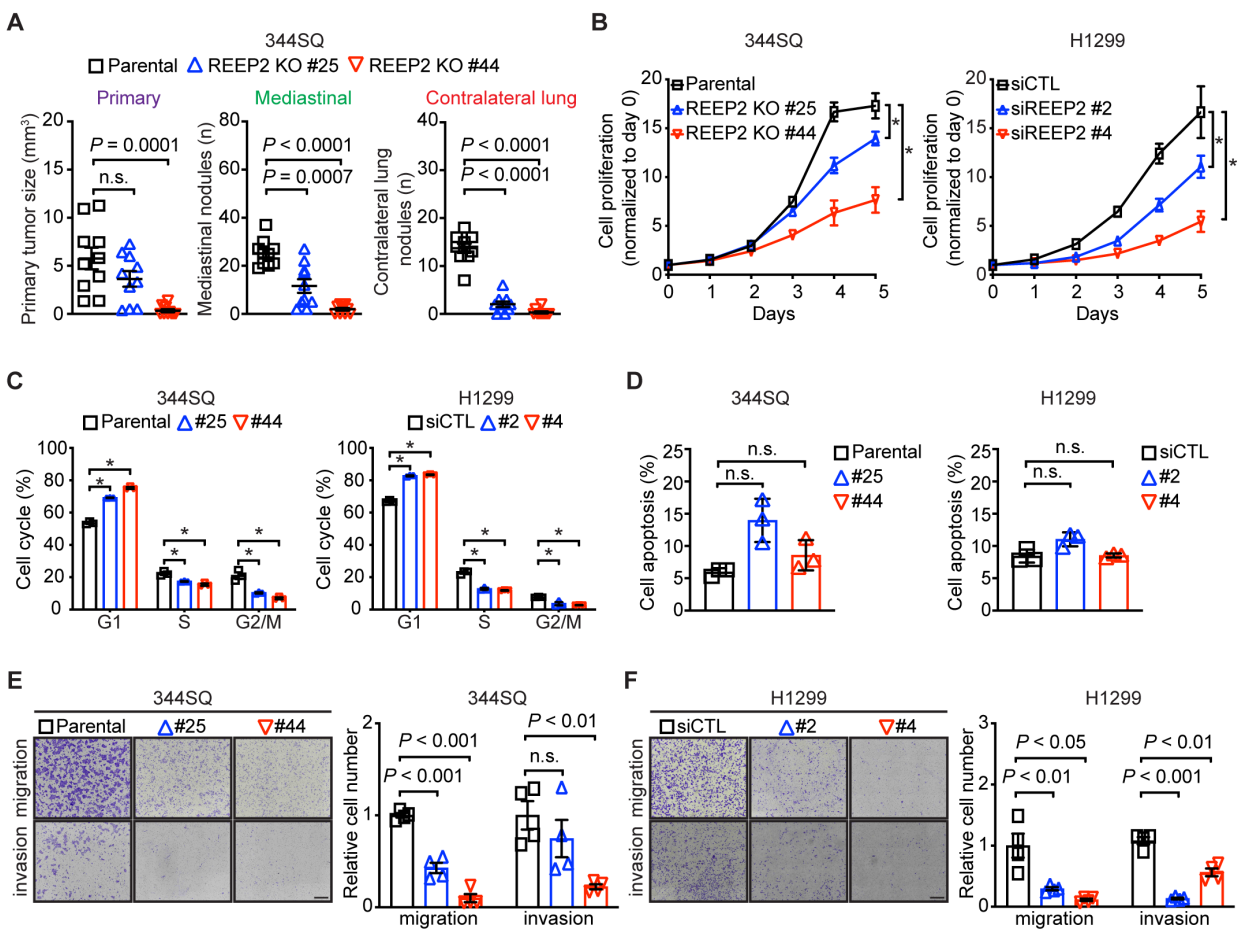

Figure 2. REEP2 is critical for EMT-driven LUAD progression. (A) Syngeneic, immunocompetent mice were injected with parental or REEP2 KO 344SQ cells and necropsies were performed 2 weeks later to assess tumor formation and metastasis (n = 10 mice per cohort). Orthotopic lung tumor size (left dot plot) and numbers of metastases to mediastinum (middle dot plot) and contralateral lung (right dot plot). (B) *In vitro* cell proliferation assay in murine 344SQ parental and REEP2 knockout (KO) cells, and human H1299 cells transfected with control siRNA (siCTL) or REEP2 siRNA (siREEP2). (C, D) Analyses of cell cycle (C) and apoptosis (D) in murine 344SQ parental and REEP2 knockout (KO) cells, and human H1299 cells with siRNA-mediated REEP2 knockdown (siREEP2). (E, F) Bright-field micrographs of crystal violet-stained murine (344SQ) (E) and human (H1299) (F) cells that migrated through noncoated (migration) or Matrigel-coated (invasion) filters in Boyden chambers. The scatter plots represent the

768 quantification of replicates 16 h after seeding and normalized to parental. Results represent

769 means ± SEM. *P* values were determined using two-tailed Student's t-test.

770

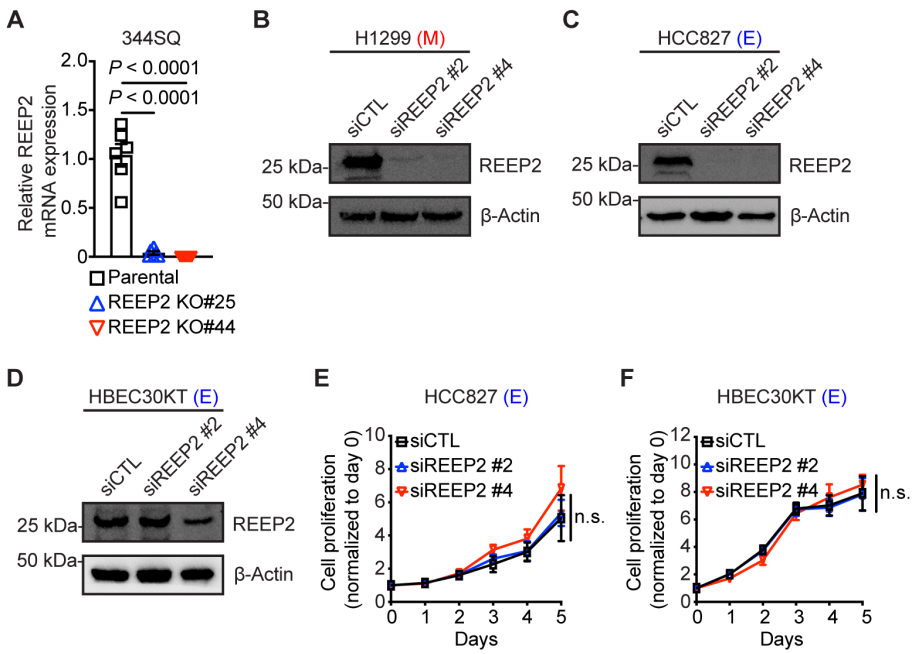

Figure S2. Depletion of REEP2 in murine and human LUAD cells. (A) qPCR analysis of REEP2 mRNA expression levels in parental or REEP2 knockout (KO) 344SQ cell lines (n=6 replicates per condition). (B-D) WB analysis of REEP2 levels in human H1299 (B), HCC827 (C), and HBEC30KT (D) cells transfected with control siRNA (siCTL) or REEP2 siRNA (siREEP2). β-Actin loading control. M: mesenchymal. E: epithelial. (E, F) *In vitro* cell proliferation assay in human HCC827 (E) and HBEC30KT (F) cells transfected with control siRNA (siCTL) or REEP2 siRNA (siREEP2). Results represent means ± SEM. *P* values were determined using two-tailed Student's t-test.

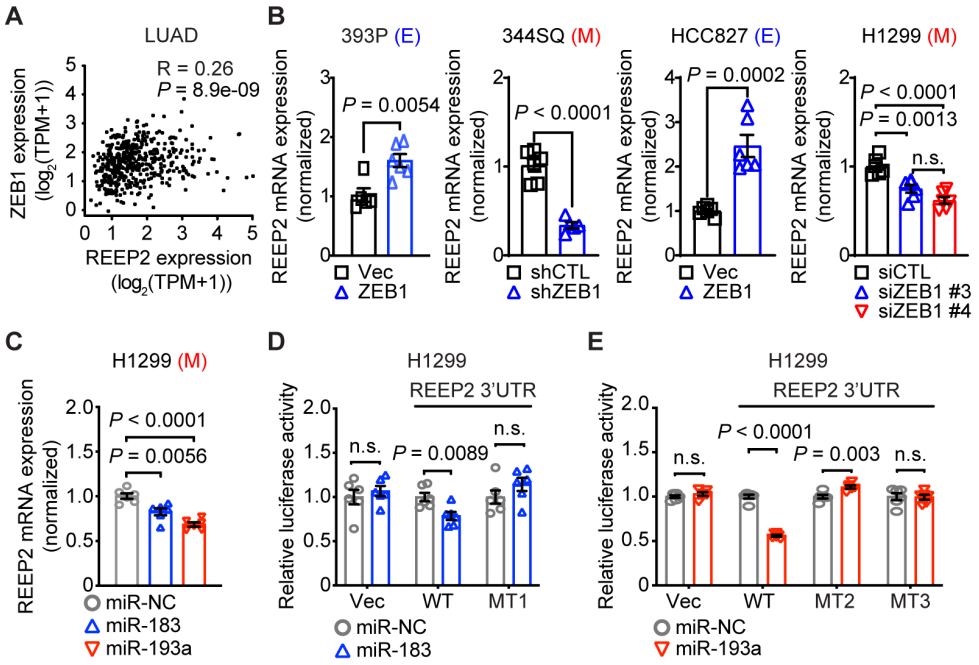

Figure 3. ZEB1 activates REEP2 via miRNAs. (A) The correlation between REEP2 and ZEB1 mRNA expression (TPM (transcripts per million)) in TCGA LUAD tissues. R, Spearman correlation. (B) qPCR analysis of REEP2 mRNA expression levels in murine (393P, 344SQ) and human (HCC827, H1299) LUAD cells with ectopic ZEB1-expression or ZEB1-depletion (n=6 replicates per condition). Vec: empty vector. E: epithelial. M: mesenchymal. (C) qPCR analysis of REEP2 mRNA expression levels in miR mimic-transfected human LUAD cells. NC: non-coding control. M: mesenchymal. (D, E) Human REEP2 3'-UTR reporter assays. Luciferase activities in H1299 cells transiently co-transfected with pre-miRs of miR-183 (D) or miR-193a (E) and human REEP2 3'UTR reporters containing wild-type (WT) or mutant 3'-UTRs lacking predicted miR-binding sites (MT1-3). Vec: empty vector. Results represent means ± SEM. *P* values were determined using two-tailed Student's t-test.

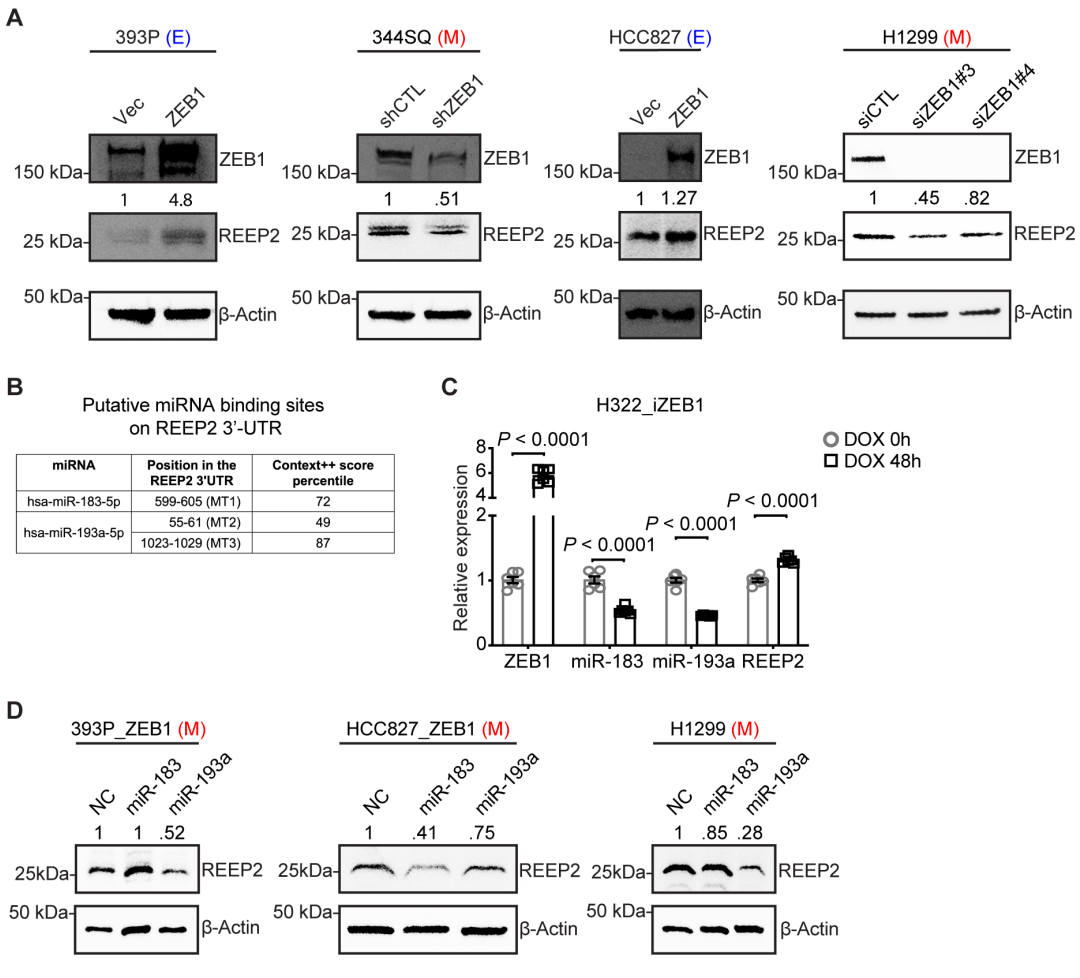

Figure S3. ZEB1 upregulates REEP2 through the regulation of miRNAs. (A) WB analysis of ZEB1 and REEP2 protein expression levels in murine (393P, 344SQ) and human (HCC827, H1299) LUAD cells with ectopic ZEB1-expression or ZEB1-depletion. β-actin loading control. Relative densitometric values are indicated. E: epithelial. M: mesenchymal. (B) Putative miRNA binding sites on REEP2 3'UTR predicted by TargetScan and used for mutagenesis (MT1-3) (C) qPCR analysis of ZEB1, miR-183, miR-193a, and REEP2 expression levels in human H322_iZEB1 cells with doxycycline (DOX) (1 μg/ml) treatment (n=6 replicates per condition). Results represent means ± SEM. *P* values were determined using two-tailed Student's t-test. (D) WB analysis of REEP2 protein expression levels in the indicated cells transfected with miR-183 or miR-193a mimics or non-coding control (NC). M: mesenchymal.

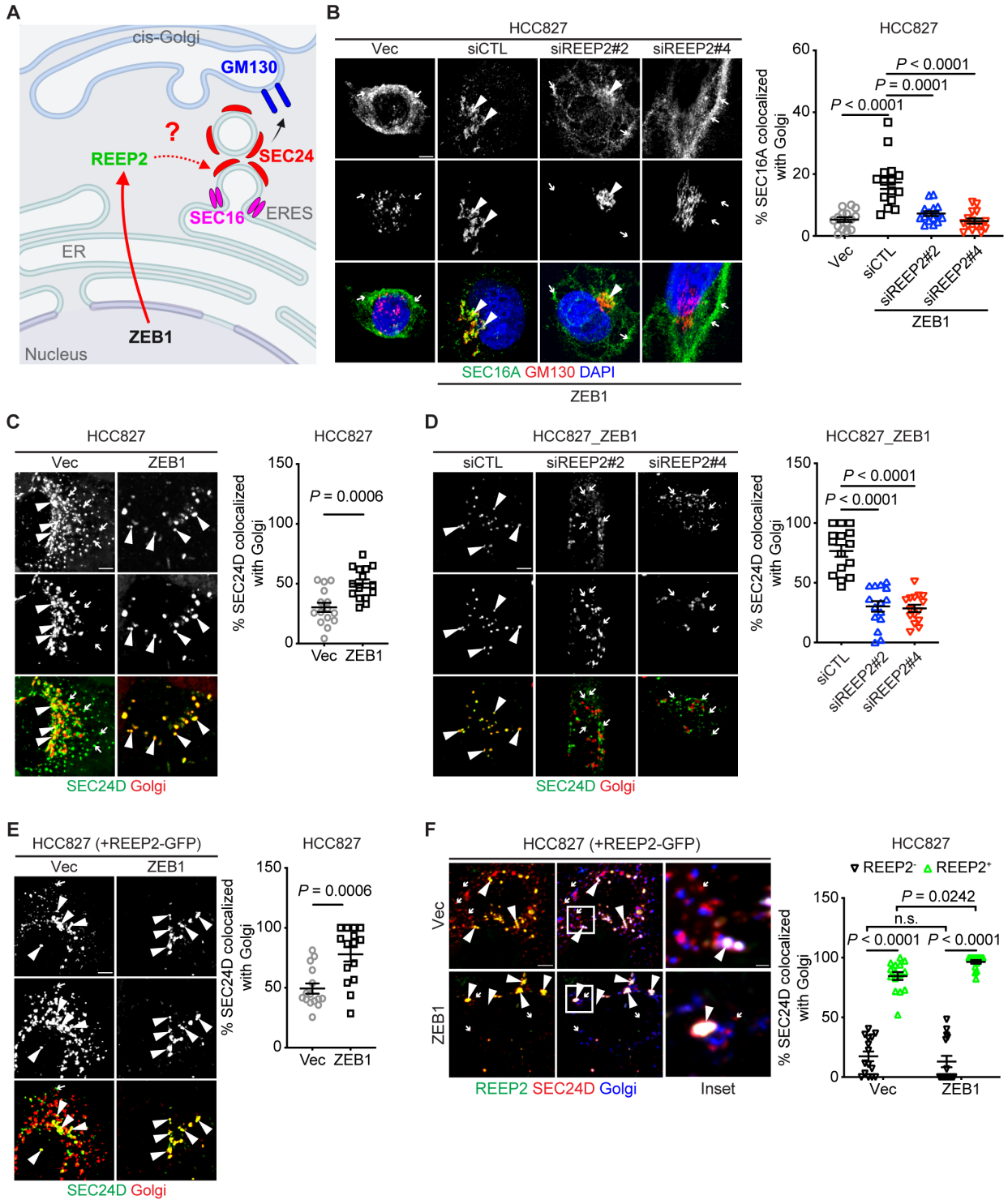

Figure 4. ZEB1 coordinates REEP2 to promote ERES colocalization with the Golgi. (A) Schematic illustration of a secretory pathway model. ZEB1 upregulates REEP2 to promote ERES (SEC16, SEC24) transportation to the Golgi (GM130). (B) Confocal micrographs of cells co-

867 stained with anti-SEC16A (green) and anti-GM130 (red) antibodies. DAPI (blue). Scale bar: 5 μm.
868 The scatter plots quantify Golgi-localized SEC16A per cell (dot) based on % of total SEC16A that
869 co-localizes with Golgi (GM130 channel) (n = 15 cells per group). (C-E) Confocal micrographs of
870 cells co-transfected with SEC24D-mCherry (green) and Golgi- pmTurquoise2 (red). DAPI (blue).
871 Scale bar: 5 μm. The scatter plots quantify Golgi-localized SEC24D per cell (dot) based on % of
872 total SEC24D that co-localizes with Golgi (n = 15 cells per group) in HCC827 cells with ectopic
873 ZEB1-expression (C), and with REEP2 depletion (D) or REEP2-GFP transfection (E). (F)
874 Confocal micrographs of cells co-transfected with REEP2-GFP (green), SEC24D-mCherry (red)
875 and Golgi- pmTurquoise2 (blue). Scale bar: 5 μm, 1 μm (inset). The scatter plots quantify Golgi-
876 localized SEC24D per cell (dot) based on % of total SEC24D that co-localizes with Golgi (n = 15
877 cells per group) in HCC827 cells with REEP2-GFP transfection. Results represent means ± SEM.
878 *P* values were determined using two-tailed Student's t-test.
879
880

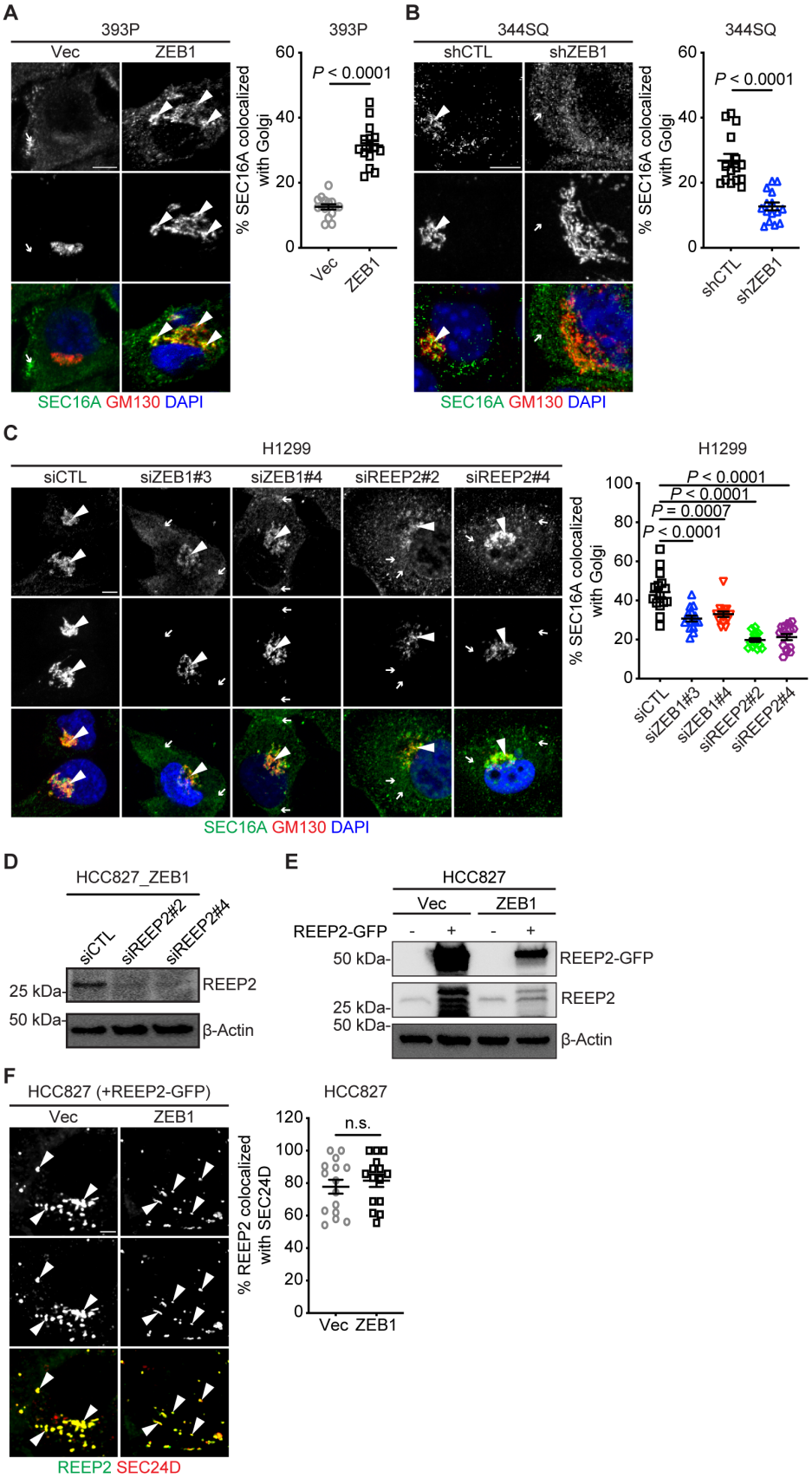
A
393P
Vec
ZEB1
% SEC16A colocalized with Golgi
P < 0.0001
SEC16A GM130 DAPI
B
344SQ
shCTL
shZEB1
C
H1299
siCTL
siZEB1#3
siZEB1#4
siREEP2#2
siREEP2#4
P < 0.0001
P = 0.0007
D
HCC827_ZEB1
25 kDa-
50 kDa-
REEP2
β-Actin
E
HCC827
REEP2-GFP
REEP2-GFP
F
HCC827 (+REEP2-GFP)
% REEP2 colocalized with SEC24D
n.s.
REEP2 SEC24D

906 **Figure S4. ZEB1 drives ERES colocalization with the Golgi via REEP2.** (A-C) Confocal
907 micrographs of cells co-stained with anti-SEC16A (green) and anti-GM130 (red) antibodies. DAPI
908 (blue). Scale bar: 5 μm. The scatter plots quantify Golgi-localized SEC16A per cell (dot) based
909 on % of total SEC16A that co-localizes with Golgi (GM130 channel) (n = 15 cells per group) in
910 murine epithelial cells (393P) with ectopic ZEB1-expression (A), in murine mesenchymal cells
911 (344SQ) with ZEB1 depletion (B), or in human mesenchymal cells (H1299) with ZEB1 or REEP2
912 depletions (C). (D) WB analysis of REEP2 protein expression levels in HCC827_ZEB1 cells
913 transfected with control siRNA (siCTL) or REEP2 siRNA (siREEP2). β-actin loading control. (E)
914 WB analysis of REEP2 protein expression levels in HCC827 cells co-transfected with empty
915 vector (Vec) or ZEB1, with REEP2-GFP. β-actin loading control. (F) Confocal micrographs of cells
916 co-transfected with REEP2-GFP (green) and SEC24D-mCherry (red). Scale bar: 5 μm. The
917 scatter plots quantify SEC24D-localized REEP2 per cell (dot) based on % of total REEP2 that co-
918 localizes with SEC24D (n = 15 cells per group) in HCC827 cells with ectopic ZEB1-expression.
919 Results represent means ± SEM. *P* values were determined using two-tailed Student's t-test.
920
921

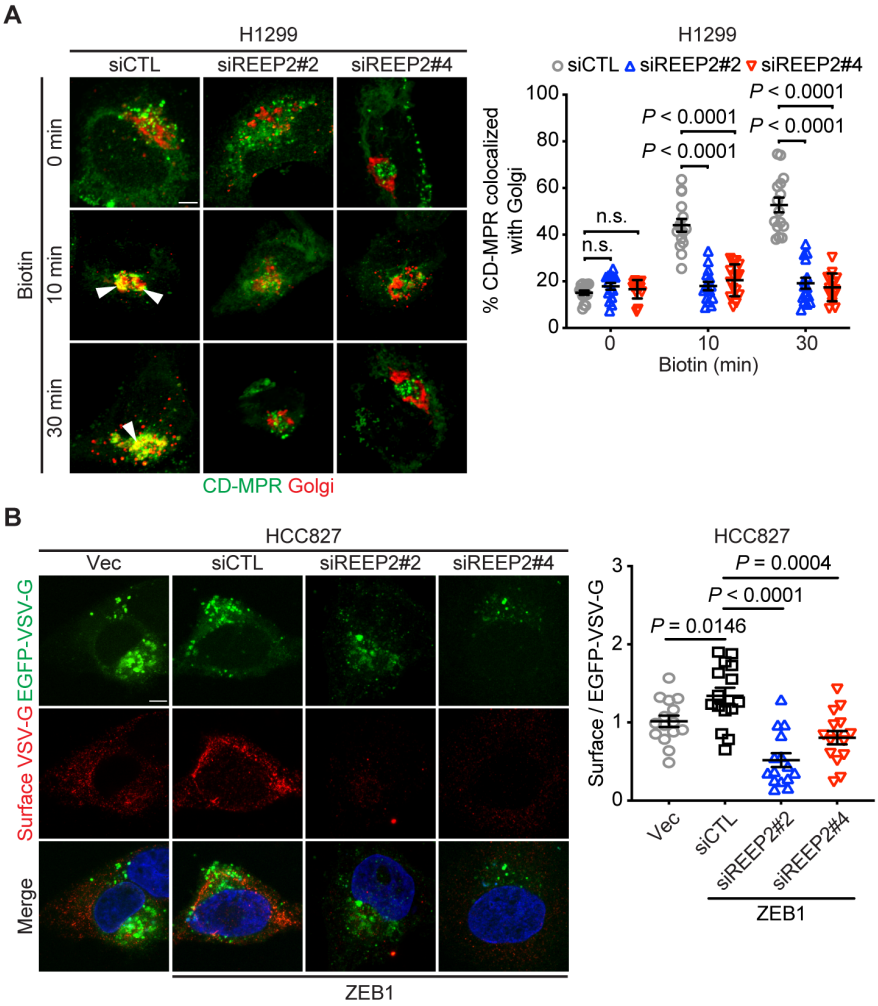

Figure 5. REEP2 promotes ER-to-Golgi trafficking. (A) Confocal micrographs of cells co-transfected with CD-MPR-RUSH-GFP (green) and Golgi-pmTurquoise2 (red). Scale bar: 5 μm. The scatter plots quantify Golgi-localized CD-MPR per cell (dot) based on % of total CD-MPR that co-localizes with Golgi at different time points after biotin treatment (40 μM) (n = 15 cells per group) in H1299 cells transfected with control siRNA (siCTL) or REEP2 siRNA (siREEP2). (B) Confocal micrographs of EGFP-VSV-G-transfected cells taken 1 h after transfer to permissive temperature. Scale bar, 5 μm. The scatter plot represents the ratio of surface VSV-G to EGFP-VSV-G in each cell (dot) (n = 15 cells per group) in HCC827 cells co-transfected with empty vector (Vec) or ZEB1 with control siRNA (siCTL) or REEP2 siRNA (siREEP2). Results represent means ± SEM. *P* values were determined using two-tailed Student's t-test.

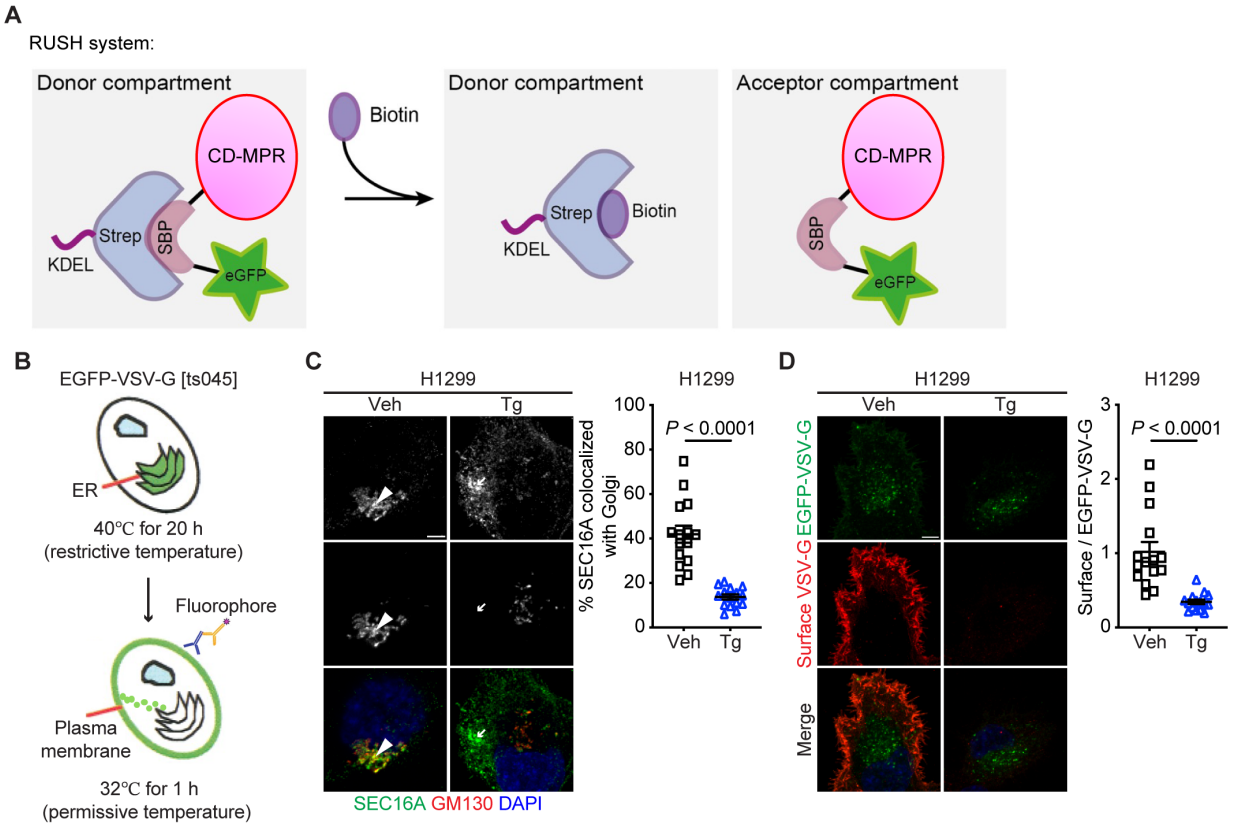

933

934 **Figure S5. ERES/Golgi colocalization promotes secretory trafficking.** (A) Schematic
935 illustration of the retention using selective hooks (RUSH) system. The cells were co-transfected
936 with the reporter protein (CD-MPR), which is fused to the streptavidin-binding peptide (SBP) and
937 GFP, and a second protein with a C-terminal ER retention signal (Lys-Asp-Glu-Leu; KDEL) fusing
938 with streptavidin as a hook. The interaction of CD-MPR with the hook protein retains CD-MPR in
939 the ER compartment and biotin administration releases the CD-MPR-GFP reporter from the ER
940 and transfers it to the Golgi. (B) Schematic of VSV-G assay. The cells were transfected with
941 vectors that express an EGFP-tagged temperature-sensitive mutant VSV-G (EGFP-VSV-G
942 [ts045]) that is transported from the ER to the plasma membrane via the Golgi. At designated time
943 points after switching cells to temperatures that cause VSV-G accumulation (40°C) and release
944 (32°C) from the ER, cells were fixed and exofacial VSV-G was detected in non-permeabilized
945 cells by staining with anti-VSV-G monoclonal antibody. The VSV-G trafficking to the plasma
946 membrane is determined by the ratio of exofacial (surface) VSV-G fluorescence signal to the

947 EGFP signal intensity. (C) Confocal micrographs of cells co-stained with anti-SEC16A (green)
948 and anti-GM130 (red) antibodies. DAPI (blue). Scale bar: 5 μm. The scatter plots quantify Golgi-
949 localized SEC16A per cell (dot) based on % of total SEC16A that co-localizes with Golgi (GM130
950 channel) (n = 15 cells per group) in H1299 cells treated with vehicle control (Veh) or 5 μM
951 thapsigargin (Tg) for 1 h. (D) Confocal micrographs of EGFP-VSV-G-transfected cells taken 1 h
952 after transfer to permissive temperature. Scale bar, 5 μm. The scatter plot represents the ratio of
953 surface VSV-G to EGFP-VSV-G in each cell (dot) (n = 15 cells per group) in H1299 cells treated
954 with vehicle control (Veh) or 5 μM thapsigargin (Tg) for 1 h. Results represent means ± SEM. *P*
955 values were determined using two-tailed Student's t-test.
956
957

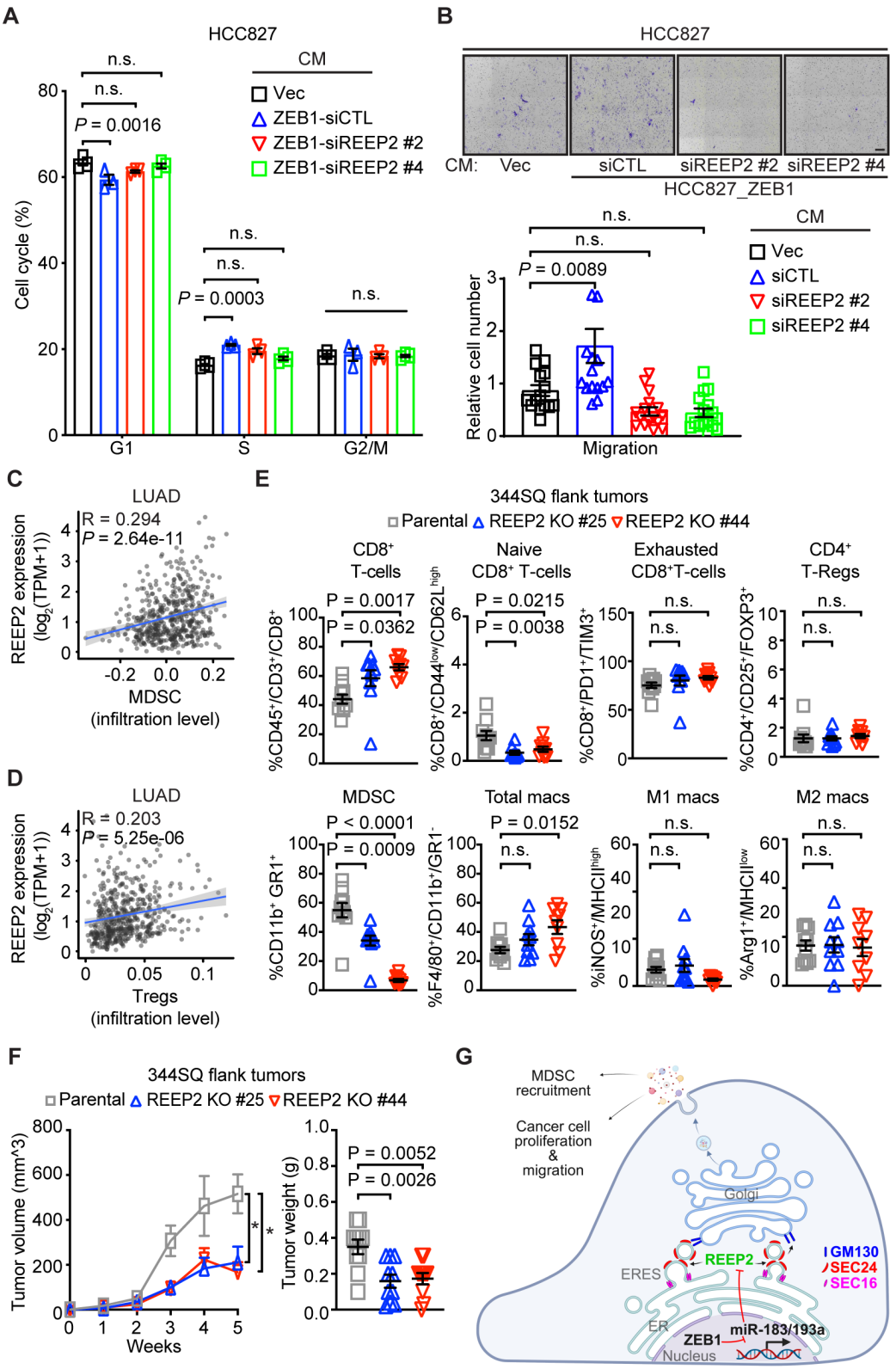

Figure 6. REEP2-driven secretome promotes LUAD progression. (A) Analyses of cell cycle in HCC827 cells treated with CM from indicated cells. (B) Bright-field micrographs of crystal violet-

984 stained HCC827 cells that migrated through noncoated filters in Boyden chambers. Upper
985 chambers loaded with indicated CM samples. The scatter plots represent the quantification of
986 replicates 16 h after seeding and normalized to Vec. (C, D) Correlation of REEP2 mRNA levels
987 with infiltration levels of myeloid-derived suppressor cells (MDSCs) (C) and regulatory T (Tregs)
988 cells (D) quantified by quanTIseq analysis in a human LUAD cohort (Data generated from
989 TIMER2.0). R, Spearman correlation. (E) Flow cytometric analysis of parental or REEP2-depleted
990 (REEP2 KO #25 or #44) 344SQ-generated flank tumors isolated from syngeneic,
991 immunocompetent mice (n = 10 tumors per cohort). Percentages of T cells ($CD8^+$ T cells,
992 $CD44^{low}/CD62L^{high}$ naïve $CD8^+$ T cells, $PD1^+/TIM3^+$ exhausted $CD8^+$ T cells and $CD25^+/FOXP3^+$
993 $CD4^+$ Treg cells), MDSCs, and antigen-presenting cells (total macrophages, M1 macrophages,
994 and M2 macrophages) were quantified. (F) Flank tumor volume (left) and weight (right) in
995 syngeneic, immunocompetent mice (dots) injected with parental or REEP2-depleted (REEP2 KO
996 #25 or #44) 344SQ cells. (G) Schematic illustration of a working model. ZEB1 relieves REEP2
997 from miR-183- and miR-193a-mediated silencing, thereby locating ERES on the Golgi and
998 facilitating pro-metastatic secretion that recruits MDSC in the TME and promotes cancer
999 progression.
1000
1001

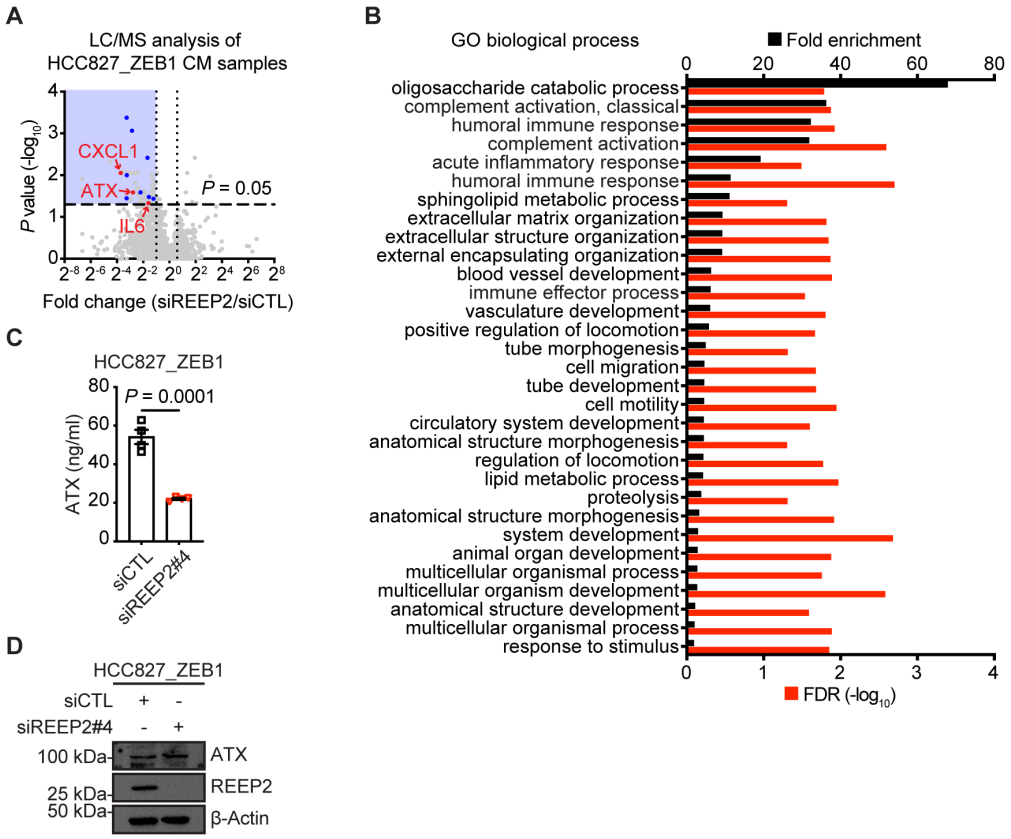

Figure S6. REEP2 activates a pro-metastatic secretion. (A) Volcano plot of proteins identified by LC/MS analysis of CM samples. *P* values (Y axis) and fold-change (X axis). Blue box indicates proteins with significantly reduced secretion (blue box, $P < 0.05$) in REEP2-depleted HCC827_ZEB1 cells (siREEP2). The blue and red dots label the factors that are associated with immune regulation. (B) Enrichment analysis (Fisher's exact test using Gene Ontology terms) of the down-regulated secreted proteins. (C) ELISA assay shows the ATX levels in CM samples (n = 4 replicates per group). *P* values were determined using two-tailed Student's t-test. (D) WB analysis of ATX and REEP2 levels in human HCC827_ZEB1 cells transfected with control siRNA (siCTL) or REEP2 siRNA (siREEP2#4). β-actin loading control.